A Computational Fluid Dynamics Investigation of Pneumatic Atomization, Aerosol Transport, and Deposition in Aerosol Jet Printing Process

Roozbeh (Ross) Salary
Department of Mechanical Engineering,
College of Engineering & Computer Sciences,
Marshall University,
Huntington, WV 25755;
Center for Advanced Microelectronics
Manufacturing,
State University of New York,
Binghamton, NY 13902

Jack P. Lombardi
Center for Advanced
Microelectronics Manufacturing,
State University of New York,
Binghamton, NY 13902

Darshana L. Weerawarne
Center for Advanced
Microelectronics Manufacturing,
State University of New York,
Binghamton, NY 13902;
Department of Physics,
University of Colombo,
Colombo 03, Sri Lanka

Prahalada Rao
Department of Mechanical and
Materials Engineering,
University of Nebraska-Lincoln,
Lincoln, NE 68588

Mark D. Poliks[1]
Center for Advanced
Microelectronics Manufacturing,
State University of New York,
Binghamton, NY 13902
e-mail: mpoliks@binghamton.edu

Aerosol jet printing (AJP) is a direct-write additive manufacturing technique, which has emerged as a high-resolution method for the fabrication of a broad spectrum of electronic devices. Despite the advantages and critical applications of AJP in the printed-electronics industry, AJP process is intrinsically unstable, complex, and prone to unexpected gradual drifts, which adversely affect the morphology and consequently the functional performance of a printed electronic device. Therefore, in situ process monitoring and control in AJP is an inevitable need. In this respect, in addition to experimental characterization of the AJP process, physical models would be required to explain the underlying aerodynamic phenomena in AJP. The goal of this research work is to establish a physics-based computational platform for prediction of aerosol flow regimes and ultimately, physics-driven control of the AJP process. In pursuit of this goal, the objective is to forward a three-dimensional (3D) compressible, turbulent, multiphase computational fluid dynamics (CFD) model to investigate the aerodynamics behind: (i) aerosol generation, (ii) aerosol transport, and (iii) aerosol deposition on a moving free surface in the AJP process. The complex geometries of the deposition head as well as the pneumatic atomizer were modeled in the ANSYS-FLUENT environment, based on patented designs in addition to accurate measurements, obtained from 3D X-ray micro-computed tomography (μ-CT) imaging. The entire volume of the constructed geometries was subsequently meshed using a mixture of smooth and soft quadrilateral elements, with consideration of layers of inflation to obtain an accurate solution near the walls. A combined approach, based on the density-based and pressure-based Navier–Stokes formation, was adopted to obtain steady-state solutions and to bring the conservation imbalances below a specified linearization tolerance (i.e., 10^{-6}). Turbulence was modeled using the realizable k-ε viscous model with scalable wall functions. A coupled two-phase flow model was, in addition, set up to track a large number of injected particles. The boundary conditions of the CFD model were defined based on experimental sensor data, recorded from the AJP control system. The accuracy of the model was validated using a factorial experiment, composed of AJ-deposition of a silver nanoparticle ink on a polyimide substrate. The outcomes of this study pave the way for the implementation of physics-driven in situ monitoring and control of AJP. [DOI: 10.1115/1.4049958]

Keywords: advanced manufacturing, aerosol jet printing (AJP), flexible and hybrid electronics, computational fluid dynamics (CFD)

1 Introduction

1.1 Motivation and Significance. Aerosol jet printing (AJP) is a droplet-based direct-write additive manufacturing process, which has emerged as a high-resolution method for the fabrication of a broad spectrum of electronics, e.g., interconnects [1–3], optical waveguides [4,5], optoelectronic devices [6–8], organic light emitting diodes [8], quantum dot devices [9,10], fine-pitch electronics [11], sensors [12,13], and transistors [14–16]. AJP has a large stand-off distance, allowing for fine material deposition and device fabrication on nonplaner surfaces (with feature sizes as small as 10 μm) [17–19]. It also accommodates a wide range of ink viscosity (approximately 1–2500 cP). This implies that novel and advanced ink materials, e.g., graphene oxide, PEDOT:PSS, carbon nanotube, and noble metal nanoparticles, can be (ultrasonically or pneumatically) nebulized and then additively deposited on a (flexible or rigid) surface toward device fabrication. The underlying physics behind ultrasonic atomization is based on high-frequency vibration, while in pneumatic atomization, a high-pressure flow of an inert gas results in droplet formation; these two mechanisms of aerosol generation will be delineated in Sec. 2. Figure 1 exemplifies flexible electronics, fabricated by the authors using the AJP process. Please note that while AJP has been reliably utilized for the fabrication of conformal electronics or printed 2-2.5D structures, complete three-dimensional (3D)-fabrication is still a looming challenge.

Despite the aforementioned unique advantages and the broad range of applications engendered by AJP, the process is highly unstable, complex, and prone to gradual drifts in machine behavior, leading to suboptimal (and sometimes unsatisfactory) material deposition and device fabrication [21,22]. Formation of overspray (and satellite particles), deposition of lines with discontinuous edges, excess generation of aerosols, and inconsistent flow collimation are examples of adverse phenomena, which cause a deviation from optimal regimes in AJP process. To a great extent,
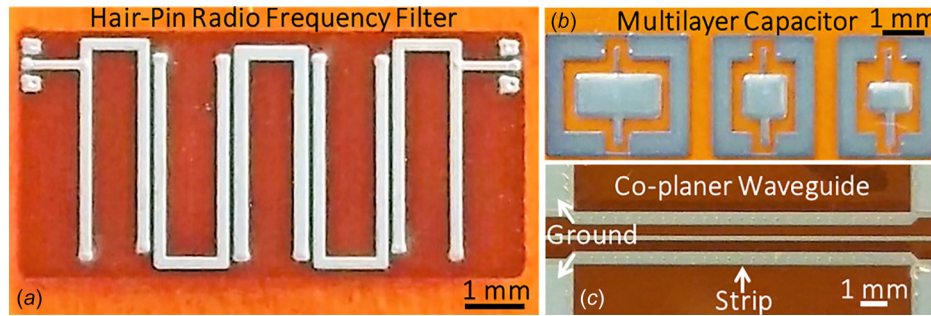

Fig. 1 Examples of electronic devices, AJ-fabricated at State University of New York (SUNY)-Binghamton. (*a*) A silver nanoparticle-based hair-pin radio frequency filter, printed on Kapton. (*b*) Multilayer capacitors, composed of silver nanoparticle and dielectric inks (layer arrangement: conductor, dielectric, conductor). (*c*) A 1-in. long coplaner waveguide structure made of silver nanoparticles on Kapton; the ground lines are connected to a conductor layer via holes (adapted from Ref. [20]).

changes in material formulation and properties are the leading cause of the AJP process complexity. The fluctuation of material properties stems from, for example, ink temperature instability as well as solvent evaporation, leading to ink predrying and/or particle accumulation within the deposition head [22,23]. Consequently, implementation of physics-driven in situ process monitoring and control in the AJP process is inevitably a need. To realize this objective, the authors have already introduced an image-based platform for near real-time process monitoring as well as closed-loop control in AJP, as delineated in Refs. [21], [22], and [24–29]. The AJP system (machine) was integrated with temporal and image-based sensors, allowing for near real-time data acquisition from the process. In addition, a wide range of digital image/signal processing and control algorithms were developed for the characterization of two-dimensional (2D) and 3D line morphology traits. Although the established platform has significantly enabled AJP process monitoring and control, the underlying aerodynamics and physical phenomena behind AJP have remained unexplored. This gap is addressed in this study, which is a direct continuation of the authors' previous works [20–22], dedicated to development of a 3D compressible, turbulent multiphase flow computational fluid dynamics (CFD) model; the aim is to investigate the underlying physical phenomena behind aerosol generation, transport, and ultimately deposition in the AJP process.

1.2 Literature Review and Identified Gaps. There are several research works, which explore various aspects of AJP process monitoring as well as material deposition.

Wang et al. [30] developed a dual-material AJP process to fabricate tunable nanocomposites, utilizing both ultrasonic and pneumatic aerosol generation methods. The process was based on two independently controlled streams of materials, mixed prior to aerodynamic collimation (in the deposition head). The dual-material process allowed for deposition of nanocomposite structures as well as real-time control of the properties of the deposited structures. In a research work by Efimov et al., the AJP process was integrated with a spark discharge generator with the aim to deposit dry silver nanoparticles (15–100 nm in diameter) on heated silicon [31] and glass [32] substrates. As a result, this process does not require postdeposition sintering. While presenting novel and original AJP-based fabrication methods, these works did not explore the physics behind particle generation, collimation, and deposition on a surface.

Gu et al. [33] presented a new process monitoring method, based on inkwells, for on-demand deposition rate measurements. Chang [34] similarly presented a process control framework, using digital image processing techniques in addition to a vibration-based wavelet method to monitor the atomization process in AJP. The method was capable of not only estimating a

stable fabrication time but also monitoring the morphology of AJ-printed structures. Using central composite design, they investigated the effects of AJP process parameters on printed line morphology. Overall, using the control framework, a 50% improvement in completion rate as well as a 20% reduction in process variation was obtained. However, no physical models were presented in their study in support of the experimental observations.

In a research work by Lombardi et al. [24], an image-based method was introduced for closed-loop control of the AJP process, including two types of controllers, i.e., proportional (P) as well as proportional-integral (PI). The aim was to control line width as a function of print speed (PS). The presented control method led to an enhancement of both linewidth and electrical properties of printed electronics. In a similar work, Thompson et al. [35] developed a velocity-regulated path planning algorithm to control the AJP process. Similarly, Smith et al. [36] presented a method for controlling the quality characteristics of AJ-fabricated flexible electronics. Sun et al. [37] developed a statistical method (processing microscopic images) for quality modeling of AJ-printed electronics. Using ensemble learning, a machine learning approach, Li et al. [38] introduced a method for AJP process monitoring and control. Verheecke et al. [39] as well as Mahajan et al. [40] demonstrated offline characterization and optimization of the AJP process for the fabrication of high-resolution silver interconnects. No physical models were discussed in all these works. Examination of the fundamental mechanisms and causes of process drifts could aid in more efficient characterization, optimization, and ultimately control of the AJP process.

Chen et al. [41] studied the effect of droplet size on overspray, an important characteristic of line morphology. In this regard, they developed a CFD model to investigate the principles of overspray formation as a function of the droplet size distribution and ShGFR.

Feng [42] studied the deformation of a sessile drop under an impinging jet. It was demonstrated that above a critical value, when viscous forces become dominant (compared to surface tension forces), unsteady droplet deformation occurs. Feng [43] also studied the dynamics of microdroplet impingement on a surface in regard to postdeposition phenomena of spreading, receding-relaxation, and wetting equilibrium. The results showed that when the influence of viscosity is negligible, periodic oscillation and aperiodic creeping-to-capillary equilibrium are discernable. In addition, contact angles as well as droplet viscosity were identified as two critical factors, influencing droplet bouncing after impingement remarkably. Feng, furthermore, investigated [44] the nature of negative pressure distribution during pneumatic aerosol generation with respect to geometric parameters, using a CFD model.

Discrete phase in a microcapillary was studied in a research work by Schulz et al. [45]. They showed that as aerosol flow

velocity increases, the Saffman force becomes significant, leading to radially inward movement of the particles within the capillary. Similarly, Akhatov et al. [46,47] demonstrated that the Saffman force, drag force, as well as particle inertia are the main factors in the modeling of aerosol flow through long microcapillaries. In another research work, Akhatov et al. [48] also presented solutions for the problem of gas flow in a slowly converging microcapillary.

Chen et al. [41] studied the effect of droplet size on overspray with the aid of a CFD model. The objective was to explain the fundamental principles governing overspray formation in AJP as a function of sheath and aerosol gas flow rates as well as droplet size distribution. In addition, the influence of particle impact velocity and aerosol flow misalignment (stemming from an internal clearance in the deposition head assembly) on the formation of overstay were investigated. They exhibited that the aerosol flow collimation is enforced by Saffman lift force, acting more significantly on larger droplets, implying that smaller droplets contribute to the formation of overspray. They emphasized the existence of a tradeoff between future size and overspray, and thus the need for optimization of the atomization process to obtain an optimum particle size distribution.

Overall, the aforementioned studies have explored various aspects of the underlying physics behind AJP. However, they are based on 2D-CFD models and/or consider a small portion of the process. In addition, a few works [44,49] have been dedicated to pneumatic nebulization in the AJP process. This work is to address these gaps by forwarding a holistic 3D-CFD model that includes not only the 3D geometry of the deposition head as well as the pneumatic atomizer completely, but also all fundamental physical models behind aerosol nebulization and deposition, such as turbulence, compressible flow, and multiphase flow.

1.3 Goal and Objective. The goal of this research work is to establish a physics-based computational platform for prediction of aerosol flow regimes (as a function of AJP process parameters) and ultimately, physics-driven control of AJP process. In pursuit of this goal, the objective of the work is to forward a multiphysics CFD model to investigate the underlying phenomena behind aerosol generation, transport, and deposition in AJP process. The aim is to explain the causal aerodynamic phenomena behind experimental observations, using a compressible, turbulent multiphase CFD model developed for the flow of aerosols: (i) during aerosolization (atomization), (ii) within the deposition head, and (iii) after deposition on a free surface. This work tests the hypothesis that the complex aerodynamic states of AJP process is captured, using a multiphysics CFD model.

The rest of the paper is organized as follows: In Sec. 2, the AJP process along with its aerodynamic components (including an ultrasonic/pneumatic atomizer, virtual impactor, and deposition head) is discussed in addition to a review of the sensor-instrumented experimental setup used in this work. The development of a 3D-CFD model is delineated in Sec. 3, consisting of geometry modeling, meshing, and setting up the governing equations. Experimental results, model validation, as well as simulation results of aerosol generation, transport, and deposition are discussed in Sec. 4. Conclusions and future work are presented in Sec. 5.

2 Aerosol Jet Printing

2.1 Process. The AJP process is centered on atomization/nebulization of an ink, which can be implemented pneumatically or ultrasonically. Figure 2 illustrates both the modes of atomization. In the pneumatic configuration, a high-pressure flow of an inert gas is injected into the ink reservoir via a head (as will be demonstrated later in Fig. 4 in Sec. 2.2) where due to the Venturi effect, the ink is drawn upward through the capillary and then sheared by the jet; as a result, a nonuniform mist/cloud of aerosols is
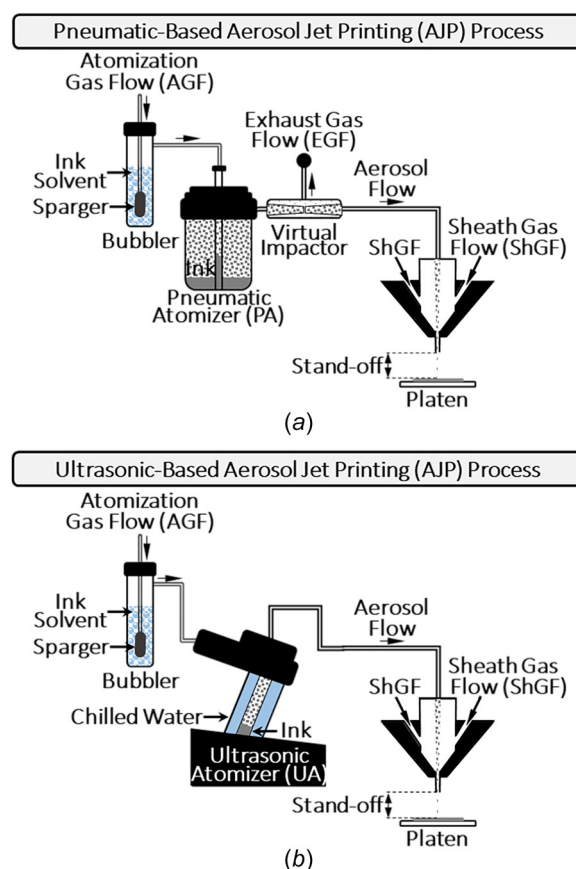

Fig. 2 Two configurations of aerosol generation in the AJP process: (a) pneumatic-based and (b) ultrasonic-based. The pneumatic atomization process further utilizes a virtual impactor to deliver a uniform flow of aerosols.

generated. Therefore, an aerodynamic separator, called the virtual impactor (VI), is utilized to filter out droplets with low linear momentum using an exhaust flow and deliver a uniform stream of aerosols for deposition. In the ultrasonic mode of atomization (UA), a transducer is used for direct aerosol/droplet formation. The temperature of the UA process is kept constant using a chilled water system to ensure uniform ink viscosity and mitigate unavoidable process drifts during the deposition of material. A bubbler filled with ink solvent(s) is used to deliver a saturated gas flow for atomization and thus to compensate for solvent evaporation. The ultrasonically generated aerosols are more uniform (and to some extent finer) than those generated pneumatically [23,50,51]; this precludes the need for a separator such as the VI in the UA mode. The mean diameters of pneumatically and ultrasonically generated aerosols are approximately $< 1\,\mu m$ and $< 0.2\,\mu m$, respectively [51]. Relatively monodisperse aerosols are generated using the ultrasonic mode of atomization, although it has limited ability to nebulize viscous materials [50]. A pneumatic nebulizer is typically used when the liquid viscosity is in the range of 20–1000 cP, and an ultrasonic atomizer is used for low viscosity fluids (1–20 cP) [51]. The uniform stream of aerosols flows toward the deposition head where a surrounding flow, called the sheath gas flow (ShGF), is introduced to collimate/focus the central aerosol flow to a narrow beam, deposited on free surface. The deposited material eventually experiences the postdeposition phenomena of spreading, receding, relaxation, and coalescence [43].

All printing experiments, discussed in the work, were carried out using an Optomec AJ-300 aerosol jet printer (Albuquerque, NM). Shown in Fig. 3, the experimental setup was further equipped with a 5 MP charge-coupled device (CCD) camera
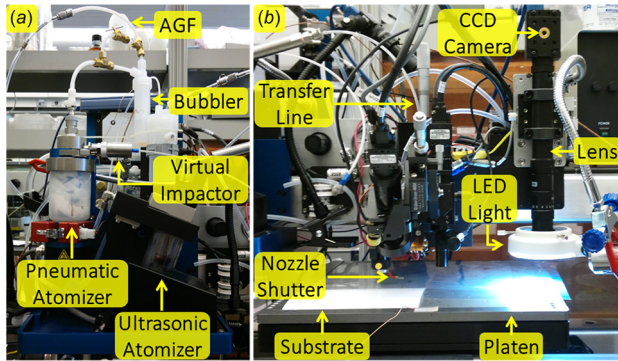
Fig. 3 The AJP experimental setup, instrumented with a high-resolution imaging system allowing for in situ image acquisition from deposited structures
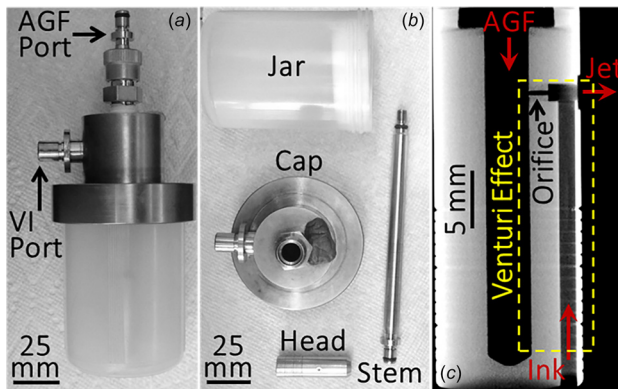

Fig. 4 (*a*) The assembled PA unit; (*b*) the main components of the pneumatic atomizer; and (*c*) obtained using X-ray computed tomography (CT) imaging, a cross section of the atomization head, showing the mechanism behind the formation of a jet of aerosols, based on the Venturi effect

Fig. 5 (*a*) The main components of the virtual impactor, (*b*) the assembled VI unit, and (*c*) an X-ray CT scan of the VI, showing the mechanism behind the aerodynamic separation of aerosols

(Edmund Optics, Grasshopper, GS3-U3-50S5C-C, Barrington, NJ), to acquire online images from the printed structures. The camera was mounted on a 2.5*X*-10*X* variable magnification lens (Edmund Optics, VZM 1000i, Barrington, NJ), illuminated by an LED ring light (AmScope, Irvine, CA). This light source has a maximum brightness of 30,000–40,000 Lux and a color temperature of 6000 K.

2.2 Pneumatic Atomizer. Demonstrated in Fig. 4, the pneumatic atomizer is composed of the following components: (i) a head with an internal capillary and an orifice, generating a multiphase jet of aerosols (based on the Venturing effect); (ii) a long stem, guiding the atomization gas flow toward the atomization head; (iii) a jar/reservoir, containing ink; and (iv) a cap, which ensures airtight operation and allows for ink temperature measurements via insertion of a thermocouple.

2.3 Virtual Impactor. Figure 5 exhibits the main complements of the virtual impactor, including: (i) an impactor, which is basically a converging nozzle; (ii) a collector, which separates aerosols based on their linear momentum as a function of the exhaust gas flow rate (we note that for the central aerosol flow, not diverted toward the exhaust, this component acts as a diffuser, resulting in a decrease in the flow velocity); (iii) a stem, guiding the aerosol flow toward the impactor; and (iv) a retaining nut and housing. The outlet stream of aerosols (more uniform in particle size) flows toward the deposition head via a polymer tube, known
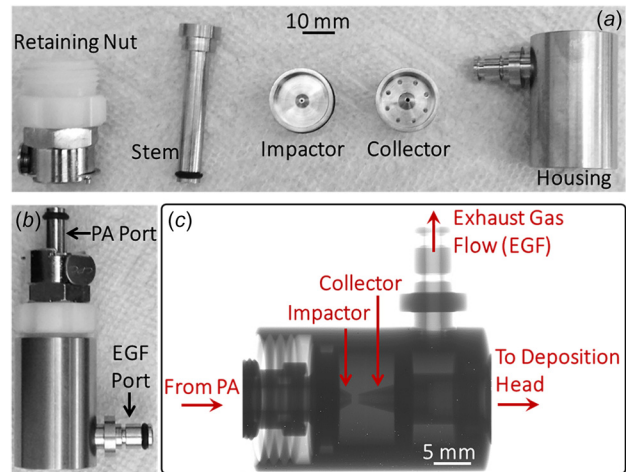
as the mist tube. Accumulation of aerosols within the tube (resulting in droplet formation and ultimately nozzle clog) is one of the main causes of anomalies in the AJP process. Consequently, purging/cleaning the mist tube regularly is a need to maintain continuous AJP operation.

2.4 Deposition Head and Nozzle. The deposition head is the last aerodynamic element in the AJP process, aiding in collimated deposition of aerosols. As demonstrated in Fig. 6, it consists of: (i) an upper plenum chamber (UPC); (ii) a lower plenum chamber (LPC); (iii) a combination chamber (CC); (iv) a long converging nozzle/microcapillary; and (v) a shell together with a retaining cap. The UPC and LPC guide the sheath gas flow toward the CC where it concentrically surrounds the aerosol flow. The collimated aerosol flow then passes through the nozzle (made up of ceramic), gaining momentum for deposition on a free surface. The exit diameter of the nozzle is an influential factor on the width and final morphology of the deposited material.

3 Development of a Computational Fluid Dynamics Model

In this section, we forward a 3D CFD model to understand the underlying dynamics behind aerosol transport and deposition in AJP, and simulate formation of line topology under various process conditions. Building a CFD model involves: (1) geometry modeling; (2) meshing; (3) setting up the governing equations; (4) specifying the boundary conditions as well as material properties; and (5) selecting numerical schemes to solve a system of coupled, linearized algebraic equations relating cell center values (having discretized the governing partial differential equations (PDEs) of the problem). We note that the discretization of the governing equations is based on finite volume method. The simulation results are verified with the physical conditions of the problem, and then validated with offline experimental measurements. The modeling and simulations presented in this study were carried out in the ANSYS-FLUENT environment (V. 16.2). The objective is to develop the numerical solution to a compressible and turbulent multiphase flow problem: (i) in the deposition head (as an internal flow problem); (ii) during deposition on a rigid and movable substrate (as an external flow problem). In general, there are two types of errors, namely, discretization and linearization. The former reduces with refining the mesh, while the latter decreases by iteration. In our simulations, a linearization tolerance of 10^{-6} was set for all conservation imbalances. This ensures obtaining an
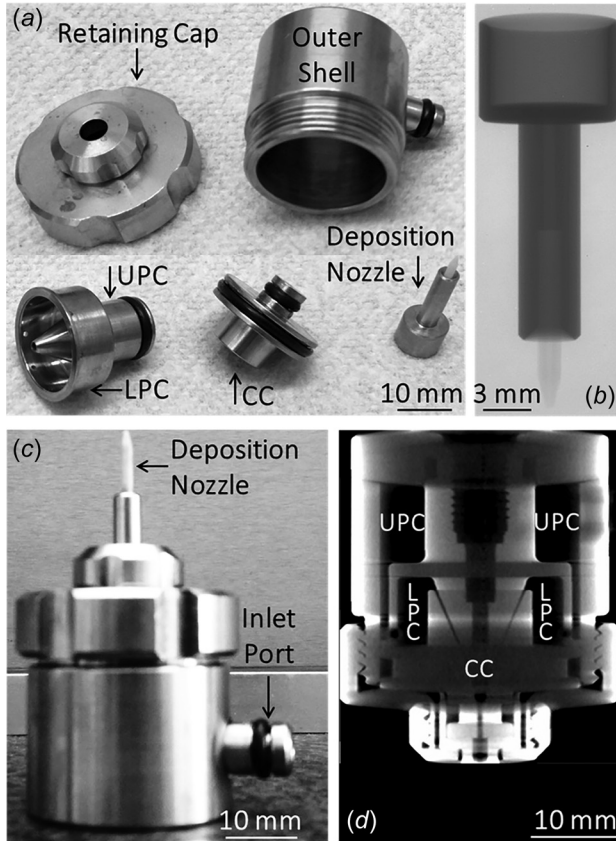
Fig. 6 (a) The main components of the deposition head, (b) a cross section of the nozzle, obtained using X-ray CT imaging, (c) the deposition head assembly, and (d) an X-ray cross section of the assembly, showing the internal structure (adapted from Refs. [22] and [26])
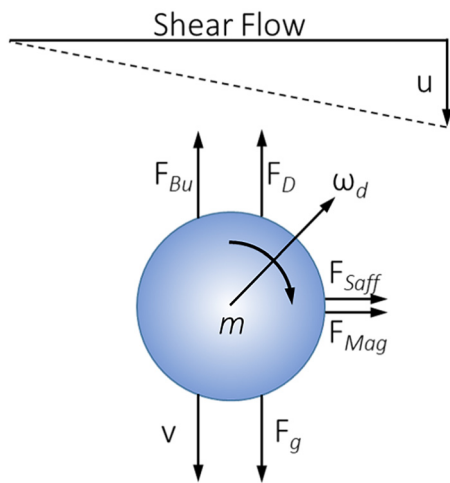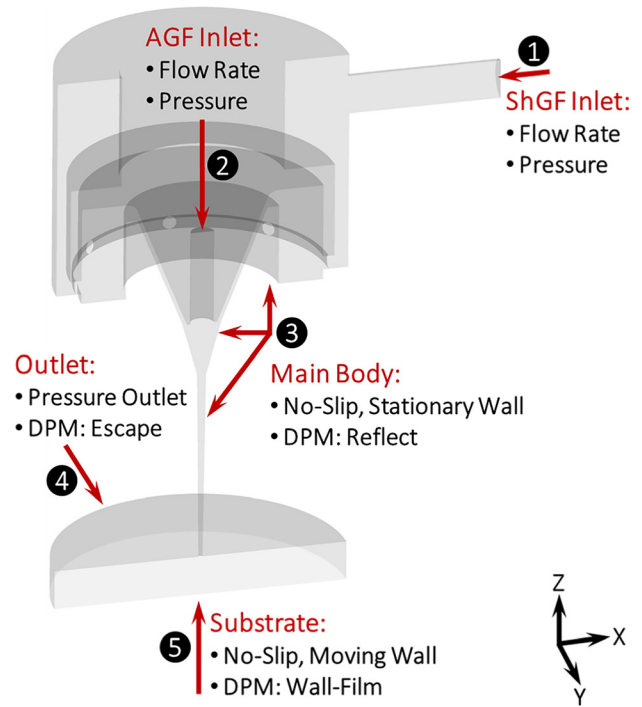

Fig. 8 A cross section of the deposition head, showing various types of boundary conditions defined for the problem of aerosol transport and deposition in the AJP process

Fig. 7 The main forces acting on an aerosol droplet in a shear flow (adapted from Refs. [22] and [26])
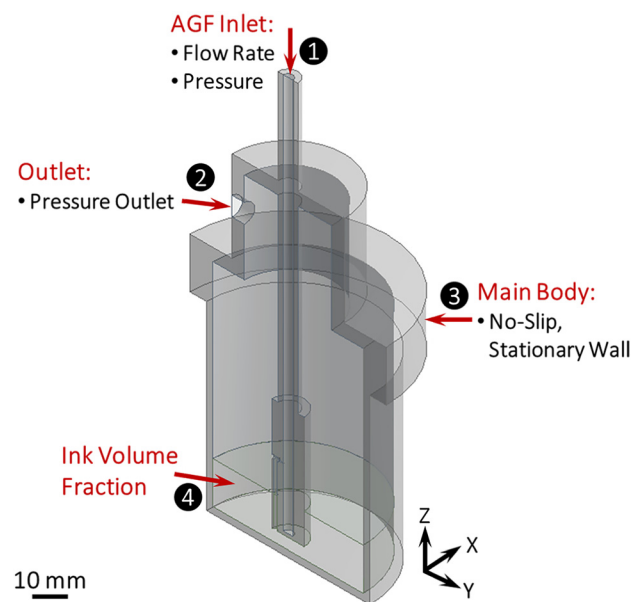

Fig. 9 A cross-sectional profile of the pneumatic atomizer along with four types of boundary conditions, including mass flow inlet, pressure outlet, and no-slip stationery wall. Volume fraction was used to define the ink volume in the flow domain.

approximate yet reliable solution to the mathematical model (consisting of the governing equations and boundary conditions).

3.1 Geometry Modeling and Meshing. The 3D geometries of the deposition head (together with its surrounding environment) as well as the pneumatic atomizer were modeled based on accurate dimensions obtained from X-ray computed tomography (CT) imaging [22] and a patented design [52] (as will be illustrated in

Figs. 8 and 9 later in Sec. 3.2.4). The geometry of the deposition head is composed of the following components: (1) ShGF inlet; (2) upper plenum chamber; (3) lower plenum chamber; (4) combination chamber; (5) nozzle; and (6) a relatively wide cylindrical volume (embedded beneath the nozzle to freely observe the effects of aerosol deposition).

The geometry of the pneumatic atomizer consists of: (1) atomization gas flow (AGF) port; (2) VI port; (3) jar/reservoir and cap

(atomization environment); (4) gas flow stem; and (5) atomization head. Carried out using a high-resolution (submicron) X-ray system (GE Phoenix Nanome|X, Niskayuna, NY), the X-ray imaging allowed for not only observation and accurate measurement of the dimensions of the internal structures (of the assemblies and their components), but also understanding the flow of material within the assemblies (which aided in defining the boundary conditions of the CFD model, e.g., the walls and internal surfaces).

The entire volume of the geometries is then meshed using a mixture of smooth and soft quadrilateral elements compiled and refined with respect to both curvature and proximity. To obtain an accurate solution near the walls, three layers of inflation were considered on all surfaces (with a geometric growth rate of 1.2). This is to ensure that equilibrium turbulent boundary layers are covered with a sufficient number of cells [53]. In general, while generating inflation layers, to some extent, aids in obtaining a more accurate solution near a surface, it may lead to poor aspect ratio and thus deterioration of mesh element quality. In fact, there is a tradeoff between the number of inflation layers and mesh aspect ratio.

The term "soft" refers to the flexible behavior of a mesh element in terms of size or the number of divisions where the element mesh size may be affected by geometry features, e.g., curvature and proximity. In contrast, the "hard" behavior of a mesh element strictly preserves the element's size or shape. The term "smooth" refers to the geometric quality of a mesh element. To obtain a smooth mesh, the location and arrangement of nodes are iteratively changed with respect to their neighboring nodes or elements [53].

3.2 Governing Equations (Mathematical Model)

3.2.1 Mass, Momentum, and Energy. A combination of density-based and pressure-based Navier–Stokes solution algorithms was used, respectively, to obtain a steady-state solution to the coupled multiphase problem, and to bring the conservation imbalances below the specified linearization tolerance (10^{-6}). Once a steady-state solution has been achieved, unsteady discrete-phase models are used to track a large number of injected particles in the system, released from the aerosol flow inlet (see Fig. 2). The conservation of energy (in addition to the conservation of mass and momentum) is added to the model as a fundamental law of fluid flow to account for the effects of compressibility at high flow velocities. Equations (1)–(4) illustrate the basic governing equations (in conservative integral form), which constitute the basis for the flow of a compressible and Newtonian fluid.

$$\text{Mass conservation}: \frac{\partial}{\partial t}\iiint_{\mathcal{V}}\rho d\mathcal{V} + \oiint_{\mathcal{A}}[\mathbf{n}.(\rho\mathbf{v})]d\mathcal{A} = 0 \quad (1)$$

$$\text{Momentum conservation}: \frac{\partial}{\partial t}\iiint_{\mathcal{V}}[(\rho\mathbf{v})]d\mathcal{V} + \oiint_{\mathcal{A}}[\mathbf{n}.(\rho\mathbf{v}.\mathbf{v})]d\mathcal{A}$$
$$= -\iiint_{\mathcal{V}}\nabla p d\mathcal{V} + \oiint_{\mathcal{A}}[\mathbf{n}.(\mu\nabla\mathbf{v})]d\mathcal{A} + \iiint_{\mathcal{V}}S_M d\mathcal{V} \quad (2)$$

$$\text{Energy conservation}: \frac{\partial}{\partial t}\iiint_{\mathcal{V}}[\rho C_v T]d\mathcal{V} + \oiint_{\mathcal{A}}[\mathbf{n}.(\rho C_v T\mathbf{v})]d\mathcal{A}$$
$$= -\iiint_{\mathcal{V}}[p\nabla.\mathbf{v}]d\mathcal{V} + \oiint_{\mathcal{A}}[\mathbf{n}.(\kappa\nabla T)]d\mathcal{A} + \iiint_{\mathcal{V}}\mathbf{\Phi}d\mathcal{V} + \iiint_{\mathcal{V}}S_E d\mathcal{V} \quad (3)$$

$$\text{Equation of state}: p = \rho RT \text{ (for perfect gas)} \quad (4)$$

In Eqs. (1)–(4), ρ is the fluid density [kg/m^3], $\mathbf{v}$ is the velocity vector [m/s], $\mathbf{n}$ is surface normal vector, p is the fluid pressure [Pa], μ is the fluid dynamic viscosity [mPa · s], C_v is the heat

capacity at constant volume [J/K], T is the fluid temperature [K], κ is the fluid thermal conductivity [W/(m K)], and R is the universal gas constant [m^3 · Pa/(K mol)]. S_M and S_E are the momentum and energy source terms, respectively. Furthermore, t, $\mathcal{V}$, and $\mathcal{A}$, are used to, respectively, represent: time, volume, and area in the integrals and partial derivatives. $\mathbf{\Phi}$ is the dissipation function, defined as follows [54]:

$$\mathbf{\Phi} = \mu\left(\begin{array}{c}2\left[\left(\frac{\partial u}{\partial x}\right)^2 + \left(\frac{\partial \mathbf{v}}{\partial y}\right)^2 + \left(\frac{\partial w}{\partial z}\right)^2\right] \\ +\left(\frac{\partial u}{\partial y} + \frac{\partial \mathbf{v}}{\partial x}\right)^2 + \left(\frac{\partial u}{\partial z} + \frac{\partial w}{\partial x}\right)^2 \\ +\left(\frac{\partial \mathbf{v}}{\partial z} + \frac{\partial w}{\partial y}\right)^2 + \frac{1}{\rho}(\nabla.\mathbf{v})^2\end{array}\right) \quad (5)$$

In Eq. (5), u, $\mathbf{v}$, and w are the x-, y-, and z-components of the velocity vector, $\mathbf{v}$, respectively.

3.2.2 Turbulence

3.2.2.1 Model. The realizable k–ε viscous model [55] utilizing scalable wall functions was used to account for the effects of turbulence—together with viscous heating/dissipation (accounted for in the energy equation, Eq. (3)), streamline curvature, and compressibility (for more accurate prediction of free shear layers)—in aerosol flow. This is because the interaction between the central aerosol flow and the focusing sheath gas flow in the deposition head results in a combined, canonical flow characterized with secondary complex features, such as streamline curvature, rotation, and vortices. The advantage of using the realizable model is that it—unlike the standard and re-normalization group models—allows for satisfaction of some mathematical constraints on the Reynolds stresses (which, by definition, reflects turbulent fluctuations in fluid momentum) [53,55]. The transport equations for the realizable k–ε model are shown in Eqs. (6) and (7)

$$\frac{\partial}{\partial t}(\rho k) + \nabla.(\rho k\mathbf{v}) = \nabla.\left[\left(\mu + \frac{\mu_t}{\text{Pr}_k}\right)\nabla k\right] - [\rho\varepsilon + \varepsilon_D]$$
$$+ \left[\mu_t S^2 - \frac{\mu_t}{\rho\text{Pr}_E}\mathbf{g}.\nabla\rho\right] + S_k \quad (6)$$

$$\frac{\partial}{\partial t}(\rho\varepsilon) + \nabla.(\rho\varepsilon\mathbf{v}) = \nabla.\left[\left(\mu + \frac{\mu_t}{\text{Pr}_\varepsilon}\right)\nabla\varepsilon\right] - \left[\rho C_{2\varepsilon}\frac{\varepsilon^2}{k + \sqrt{\frac{\mu}{\rho}\varepsilon}}\right]$$
$$- \left[C_{1\varepsilon}\frac{\varepsilon}{k}C_{3\varepsilon}\frac{\mu_t}{\rho\text{Pr}_E}\mathbf{g}.\nabla\rho\right]$$
$$+ \left[\rho\left\{\max\left(0.43, \frac{S\frac{k}{\varepsilon}}{S\frac{k}{\varepsilon} + 5}\right)\right\}S\varepsilon\right] + S_\varepsilon \quad (7)$$

where k is the fluid turbulence kinetic energy [J/kg]; μ_t is the turbulent/eddy viscosity [kg/(s.m)]; Pr_k and Pr_ε are the turbulent Prandtl numbers for the turbulence kinetic energy and dissipation rate, respectively (Prandtl number is a dimensionless number, representing the ratio of viscous diffusion to thermal diffusion); ε is the turbulence dissipation rate [J/(kg.s)]; ε_D is the rate of dissipation resulting from the fluctuating dilatation of compressible turbulence [J/(kg.s)]; S_k and S_ε are the turbulence kinetic energy and dissipation rate source terms, respectively. Note that Pr_E is the turbulent Prandtl number for fluid energy. For the realizable k-ε turbulent model, $\text{Pr}_k = 0.82$, $\text{Pr}_\varepsilon = 1.0$, and $\text{Pr}_E = 0.85$ [53]. The rate of strain of fluid elements is defined as: $S = \sqrt{2S_{ij}S_{ij}}$ where

$S_{ij} = 0.5(\nabla \mathbf{v} + \nabla \mathbf{v^T})$. Furthermore, $C_{1\varepsilon} = 1.44$ and $C_{2\varepsilon} = 1.92$, while $C_{3\varepsilon}$ is evaluated on the basis of the local flow direction (relative to the gravitational vector) [53]. In Eqs. (6) and (7), starting from the left-hand side, the first term—also known as the unsteady term—represents the rate of change of turbulence kinetic energy (k) and dissipation rate (ε), respectively; similarly, the second and third terms reflect the convection and diffusion transport, correspondingly; the fourth term is the rate of destruction; and the other remaining terms indicate the rate of production as well as sources. Compared to other k–ε models, the realizable model reflects the spectral energy transfer more properly; this can be implicitly realized by looking at the sixth term of Eq. (7), i.e., $\rho \left\{ \max\left(0.43, \frac{S\frac{k}{\varepsilon}}{S\frac{k}{\varepsilon}+5} \right) \right\} S\varepsilon$, where there is no dependency on the eddy viscosity (μ_t) and thus, on the generation of turbulence kinetic energy. Note that the destruction term in Eq. (7), i.e., $\rho C_{2\varepsilon} \frac{\varepsilon^2}{k+\sqrt{\frac{\mu}{\rho}\varepsilon}}$, is not of singularity (because of $\sqrt{\frac{\mu}{\rho}}\varepsilon$ in the denominator).

Once both k and ε have been obtained, the eddy viscosity—assumed to be an isotropic scalar quantity and work well for jet flows where only one of the turbulent shear stresses dominates [53]—is updated using Eq. (8), as follows:

$$\mu_t = \rho \frac{k^2}{\varepsilon} * \left(\frac{\left[2.45\cos\left(0.33\cos^{-1}\left(2.45 \frac{S_{ij}S_{jk}S_{ki}}{(S_{ij}S_{ij})^{\frac{3}{2}}} \right) \right) \right]}{\left[\frac{k\sqrt{S_{ij}S_{ij} + \left(\overline{\Omega_{ij}} - \varepsilon_{ijk}\omega_k - 2\varepsilon_{ijk}\omega_k \right) \left(\overline{\Omega_{ij}} - \varepsilon_{ijk}\omega_k - 2\varepsilon_{ijk}\omega_k \right)}}{\varepsilon} \right] + 4.04} \right)^{-1}$$

$$(8)$$

We note that the whole term inside the outermost parentheses (called F_μ hereafter) is constant in the standard k–ε viscous model, while here is a complex function of $\overline{\Omega_{ij}}$ as well as ω_k—in addition to k and ε known as the turbulence fields—which are the mean rate of rotation tensor and angular velocity of the system of rotation (moving reference frame), respectively.

3.2.2.2 Near-Wall Treatment. In this study, we used scalable wall functions [53] to more accurately account for near-wall effects on aerosol deposition in the presence of turbulence. Based on the law of the wall [56], the flow and turbulence parameters are expressed as a logarithmic function of the distance from the wall, y (or y^* in nondimensionalized form) as shown in Eq. (9). Subsequently, a constraint is introduced, which prevents the wall functions from deterioration in situations where y^* falls below a certain threshold as a result of grid refinement (i.e., when $y^* \leq 11.225$) [53], as mathematically stated by Eq. (10). We note that the imposed constraint on y^* (shown in this section for momentum transport) is similarly applied to standard energy and turbulence wall functions

$$\frac{v C_\mu^{0.25} k^{0.5}}{\tau_w / \rho} = 2.39 \ln(9.79 y^*) \qquad (9)$$

$$y^* = \max\left[\left(\frac{\rho C_\mu^{0.25} k^{0.5} y}{\mu} \right), 11.225 \right] \qquad (10)$$

In Eqs. (9) and (10), v is the mean fluid velocity at a wall-adjacent cell of interest [m/s]; C_μ is the turbulent viscosity constant; k is the fluid turbulence kinetic energy at the wall-adjacent cell of interest [J/kg]; τ_w is the wall shear stress [kg/(m.s²)] defined based on Newton's law of viscosity as

$\tau_w = \mu \left(\frac{\partial u}{\partial y} \right)_{y=0}$ where u and y are the x-component of velocity and the distance from the wall [m], respectively. Similarly, y^* represents the nondimensionalized distance from the wall. ρ is the fluid density [kg/m³], and μ is the fluid dynamic viscosity [mPa · s]. The term on the left hand-side of Eq. (9), i.e., $\frac{v C_\mu^{0.25} k^{0.5}}{\tau_w / \rho}$, represents nondimensionalized velocity as a lumped combination of the flow and turbulence parameters.

3.2.3 Discrete-Phase Modeling. A coupled two-phase flow model (allowing for interphase exchanges of mass, momentum, and energy between the continuous and discrete phases) was established with the aim for: (i) steady/unsteady particle tracking in the system and (ii) simulation and characterization of particle deposition under various process conditions. All of our discrete-phase simulations and calculations of particle trajectories were performed, having obtained a fully converged continuous-phase flow field.

Particle trajectories are calculated by time integration of the force balance equation—i.e., Eq. (11), based on Newton's second law of motion written in a Lagrangian frame of reference—where the forces acting on the particle are equated with the particle acceleration

$$\frac{\partial \mathbf{v}_D}{\partial t} = \begin{bmatrix} \mathbf{F}_g + \mathbf{F}_{Dg} + \mathbf{F}_{SL} \\ + \mathbf{F}_{VM} + \mathbf{F}_{PG} + \mathbf{F}_{\mathbf{Others}} \end{bmatrix} \qquad (11)$$

In Eq. (11), $\mathbf{v}_D$ is the discrete-phase/particle velocity vector [m/s]. In addition, $\mathbf{F}_g + \mathbf{F}_{Dg} + \mathbf{F}_{SL} + \mathbf{F}_{VM} + \mathbf{F}_{PG}$ represent the gravitational, drag, Saffman lift, virtual mass, and pressure gradient forces per unit particle mass, correspondingly. Figure 7 demonstrates the main forces acting on a droplet in a shear flow. The gravitational force (per unit mass), $\mathbf{F}_g$, equals $\mathbf{g}(\rho_D - \rho)/\rho_D$ where ρ_D represents the particle density [kg/m³]. Similarly, the drag force, $\mathbf{F}_{Dg}$, can be further defined as [53]

$$\mathbf{F}_{Dg} = \frac{\mathbf{v} - \mathbf{v}_D}{\left(\frac{24 \rho_D d_D^2}{18 \mu C_{Dg} \mathrm{Re}} \right)} \qquad (12)$$

where d_D is the particle diameter [m], C_{Dg} is the drag coefficient, and Re is Reynolds number. The denominator in the right-hand side of Eq. (12) is termed as the particle relaxation time [57]. The Saffman lift force, $\mathbf{F}_{SL}$, reflecting the lift acting on a small spherical particle in a slow shear flow [58,59], is given by Eq. (13). Akhatov et al. [45–47,50] demonstrated the significance of this force in modeling of high-velocity transport and deposition of droplets through long microcapillaries.

$$\mathbf{F}_{SL} = \frac{5.2 \rho \sqrt{\frac{\mu}{\rho}} (S_{ij})(\mathbf{v} - \mathbf{v}_D)}{\rho_D d_D (S_{nm} S_{mn})^{0.25}} \qquad (13)$$

Mathematically expressed by Eqs. (14) and (15), the virtual mass, $\mathbf{F}_{VM}$, and pressure gradient, $\mathbf{F}_{PG}$, forces can be ignored in situations where the density of the continuous phase is remarkably lower than that of the discrete phase (i.e., $\rho/\rho_D \ll 1$) [53]. In Eq. (14), C_{VM} represents the virtual mass factor, set at 0.5 in this study. A more detailed review of forces acting on a microdroplet is given as part of one of our previous publications on AJP [22].

$$\mathbf{F}_{VM} = C_{VM} \frac{\rho}{\rho_D} \left(\mathbf{v}_D \nabla \mathbf{v} - \frac{d\mathbf{v}_D}{dt} \right) \qquad (14)$$

$$\mathbf{F}_{PG} = \frac{\rho}{\rho_D} \mathbf{v}_D \nabla \mathbf{v} \qquad (15)$$

3.2.4 Boundary Conditions

3.2.4.1 Deposition Head. Illustrated in Fig. 8, the following boundary conditions were defined for the transport and deposition of aerosols in the AJP process, modeled as a compressible, turbulent multiphase flow problem.

(1) *Mass flow inlet* was the type of boundary set for the sheath gas flow (ShGF), being in absolute frame of reference. Based upon experimental sensor data (directly obtained from the Optomec AJ printer's data logger), both mass flow rate and gauge pressure were set as a function of the ShGFR. In addition, two turbulence parameters, i.e., turbulent intensity and turbulent viscosity ratio, were set at 1.5% and 10, respectively. The thermal condition of the inlet ShGF imposed a temperature of 300K.

(2) *Mass flow inlet* was similarly chosen for the AGF. The mass flow rate and gage pressure were set according to the experimental data. The same turbulence parameters and thermal condition as the first boundary conditions were used.

(3) *Stationery wall* with no-slip condition using the standard roughness model (having a roughness constant of 0.5) was the type of boundary set for the main body of the deposition head, which also includes the combination chamber as well as the nozzle (all being at 300K). Furthermore, "reflect" condition was the type of boundary set for the discrete phase model (DPM), utilizing the generic erosion model with a friction coefficient of 0.2.

(4) *Pressure outlet* was the boundary of choice for the atmospheric environment surrounding the jet of aerosols depositing on the substrate, with "escape" condition for the DPM. The turbulence component of the boundary was defined using backflow turbulent intensity and viscosity ratio, set at 1.5% and 10, respectively (similar to the inlet conditions).

(5) *Moving wall* with no-slip condition (utilizing the standard roughness model) was chosen to reflect the substrate conditions. In addition, "wall-film" condition was the type of boundary set for the discrete phase where the particle–substrate interactions—including four regimes of sticking, rebounding, spreading, and splashing [53]—were estimated using Stanton-Rutland model.

3.2.4.2 Pneumatic Atomizer. Illustrated in Fig. 9, the following boundary types were defined in the CFD model, reflecting the governing conditions of pneumatic atomization in AJP:

(1) *Mass flow inlet* was the type of boundary defined for the AGF. The first phase's flow rate (i.e., nitrogen) as well as the flow pressure was set based on experimental sensor data (from Optomec AJ's data logger). In addition, the second phase's flow rate (i.e., functional ink's) was set to zero at this boundary.

(2) *Pressure outlet* was the type of boundary defined for the pneumatic atomizer's exit flow.

(3) *Stationery wall* with no-slip condition was defined for: (i) the body of the atomizer, (ii) the stem, and (iii) the head (see Sec. 2.2).

(4) *A volume fraction* of 1 (i.e., 100% liquid) was patched for the ink volume to enforce the presence of the ink in the atomizer prior to simulation.

Please note that in the case of the UA, the CFD model would be changed in a twofold manner: (i) change in the geometry (see Fig. 2) and (ii) change in the mathematical model (including the governing equations and the boundary conditions, delineated in Sec. 3.2). The underlying physics behind the UA process is based on high-frequency vibration and thus generation of capillary waves (where the amplitude is the driving mechanism for aerosol generation). The frequency of vibration in addition to surface tension and fluid viscosity are the governing variables in the UA

process. Hence, not only would the fundamental transport equations—i.e., the Naiver–Stokes equations, the continuity equation, the energy equation, the equation of state, as well as the equations used for turbulence and discrete-phase modeling—be used, but also the physical equations capturing high-frequency vibration and capillary wave formation would be an integral part of the mathematical model.

4 Experimental Results

4.1 Materials. Supplied in-house, both sheath and atomization gas flows are composed of a pure (4.8 grade) and dry stream of nitrogen, flowing at ambient temperature (21 °C). The electronic structures were deposited on a flexible substrate, made up of polyimide (UPILEX 125S, Ube Plastics, Tokyo, Japan). A silver nanoparticle ink (Paru Co., Seoul, South Korea), having a particle size of 80 ± 10 nm, was used for printing four-point probe test structures (delineated in Sec. 4.2). The ink consists of the following components, mixed with a ratio of 5:1 by weight, respectively:

(i) MicroPEPG007MOP: This part is composed of silver nanoparticles (~66 wt%) and 1-methoxy-2-propanol (MOP) as solvent, and has a bulk density and viscosity of 1.5–2.5 g/ml and 50 cP, respectively.

(ii) MicroPEPG007EG: This part is composed of silver nanoparticles (~33 wt%) and ethylene glycol (EG) as solvent, and has a bulk density and viscosity of 1.2–3.3 g/ml and 39 cP, respectively.

4.2 Design and Analysis of Experiments. Detailed in Table 1, a single-factor factorial experiment was designed and conducted with the objective: (i) to investigate the influence of ShGFR on line morphology and (ii) to validate the CFD model. In this experiment, the ShGFR was randomly changed at four levels of 40, 60, 80, and 100 standard cubic centimeter per minute (sccm). Each treatment combination of the experimental design was repeated three times. Atomization gas flow rate (AGFR) and exhaust gas flow rate (EGFR) were set at 500 sccm and 450 sccm, respectively; as a result, an aerosol flow rate of 20 sccm was obtained. Utilizing the pneumatic atomizer and a 300 μm nozzle, silver nanoparticle-based devices (illustrated in Fig. 10) were printed on a polyimide substrate (nitrogen-dried, having rinsed with isopropyl alcohol and acetone) at a speed of 4 mm/s. Working distance/standoff, i.e., the distance between the nozzle and the platen, was set at 3 mm. Subsequent to printing, the devices were sintered in a convection oven (Binder, Inc., Bohemia, NY) at 200 °C for 1 h. A 5-min equilibration time was taken between each set point change to obtain a steady-state flow of material. Prior to printing, the ink was ultrasonically sonicated for approximately 2 min to ensure uniform dispersion of particles in the ink medium. Leading to an optimal process operability regime, the aforementioned process parameters were selected on the basis of a

Table 1 Details of the designed experiment conducted to systematically investigate the influence of ShGFR on line morphology

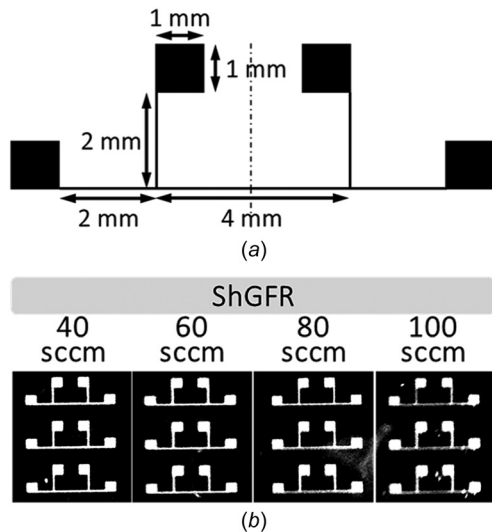| Parameter	Value
ShGFR (sccm)	40, 60, 80, and 100
EGFR (sccm)	450
PS (mm/s)	4
AGFR (sccm)	500
Atomizer type	Pneumatic
Nozzle size (μm)	300
Working distance (mm)	3
Ink	Silver NP
Substrate	Polyimide
Sintering type	Oven (1 h at 200 °C)

Fig. 10 (*a*) The dimensions of the electronic devices, deposited using AJP and (*b*) the experimental design structure together with real pictures of the printed devices

Fig. 12 Validation of the CFD simulation of line width versus ShGFR with both online and offline experimental measurements

review of literature as well as the authors' prior experimental observations as delineated in Refs. [20–22].

From the fluid dynamics perspective, the nozzle size (diameter) directly affects: (i) the flow of aerosols in the deposition head, (ii) the width of the collimated jet of aerosols issuing from the nozzle exit, and ultimately, and (iii) the width of the deposited material (i.e., line width). Particle coalescence is the primary mechanism of line formation on a free surface, followed by spreading, receding, relaxation, and wetting equilibrium [43]. The impact of nozzle size on deposited line width was studied by Mahajan et al. [40]; it was observed that the line width declined with a decrease in the nozzle diameter (from $200\,\mu m$ to $100\,\mu m$).

4.3 Validation of the Computational Fluid Dynamics Model.
Using the high-resolution imaging system (delineated in Sec. 2.1), online images were acquired from the central trace/line of each printed device, as exemplified in Fig. 11. It is evident that as the ShGFR increases from 40 sccm to 100 sccm, the line width decreases. This implies that under steady aerosol generation and transfer, thicker lines are deposited as a result of the increase in the ShGFR. No significant amount of overspray was observed in the range of 40–100 sccm. This is an indication of stable and collimated material deposition.
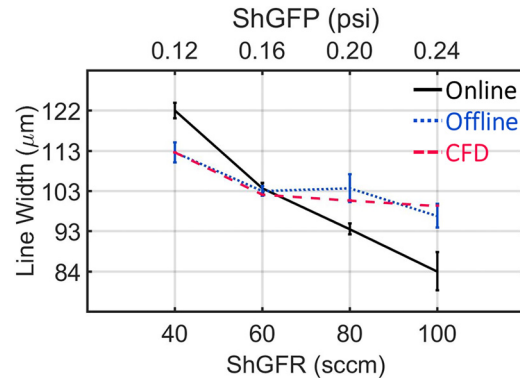
Using the 3D-CFD model forwarded in this study, the collimated deposition of aerosols on a free surface was simulated at the four levels of the ShGFR, as demonstrated later in Sec. 4.5. The changes in the line width were contrasted against both online and offline experimental observations, plotted in Fig. 12. The online measurements were based on the images captured using the CCD camera (discussed in Sec. 2.1). Similarly, the offline measurements were based on high-resolution images acquired using an optical microscope (Carl Zeiss M1M Axio Imager, Oberkochen, Germany). The online, offline, and CFD characterization of line width was carried out based on an algorithm (developed in MATLAB and PYTHON), which would analyze an image or the spatial coordinates of a line and subsequently calculate the average line width on the basis of individual column-by-column (or pixel-by-pixel) line widths, having detected the line edges, as delineated in Ref. [22].

The trend estimated by the CFD model closely mimics that of the offline measurements. In other words, there is not statistically significant difference between the two trends ($\rho = 0.93$ where ρ is the Pearson correlation coefficient). We note that the trend captured by the online images is slightly different, stemming from the image-based measurements of the line width. The difference between the online and offline measurements (which are based on CCD camera and microscope images, respectively) arises from different image properties. The difference, to a great extent, stems from the less accurately defined line edges in the CCD images. In addition, the intrinsic time difference between the online and offline image acquisition leads to different physical properties due to, for example, solvent evaporation and drying, perceived as different line widths [22,60].
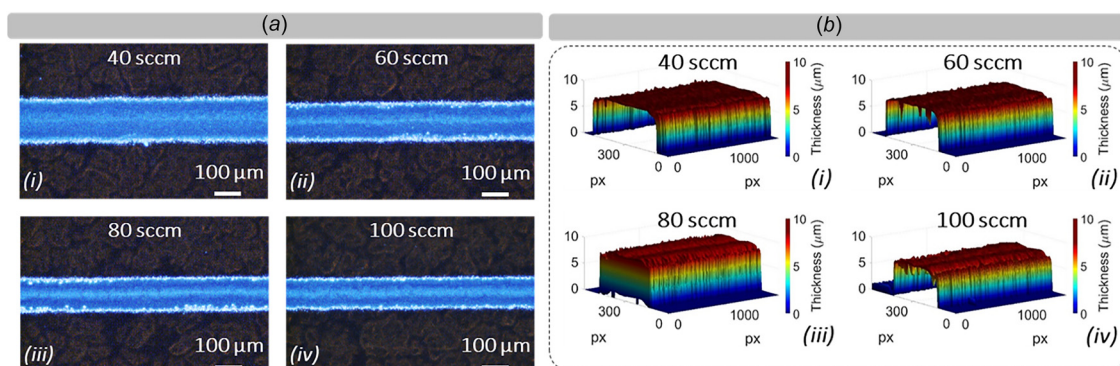

Fig. 11 Influence of the ShGFR (being in the range of 40–100 sccm) on: (*a*) the 2D and (*b*) the 3D morphological characteristics of the AJ-deposited lines. An increase in the ShGFR leads to deposition of narrower lines. Insignificant overspray formation is indicative of stable, collimated aerosol deposition. The 3D profiles were reconstructed using the shape-from-shading method [21,22].

During the aerosol transport process, losses can occur due to, for example, aerosol settlement and/or diffusion, which affect the transport efficiency, the flow rate, and ultimately the scalability of the process. It was observed, based on the authors' experimental observations, that losses significantly occur in the transfer line, known as the mist tube (see Fig. 3), during the aerosol transport process. To minimize the adverse effects of aerosol settlement in the mist tube during the validation experiment and to ensure repeatability of the results, the mist tube was cleaned prior to the experiment. The combined material transport and deposition efficiency were monitored by in situ quantification of the morphology of the deposited material with the aid of image acquisition and processing (as illustrated in Figs. 11 and 12). The CFD model was established on the basis of the assumption that the material transport losses would be negligible for short material deposition simulations (typically less than 10 s) once steady-state conditions have been reached.

The CFD model is utilized to investigate the influence of the ShGFR on the flow of aerosols within the deposition head and on the collimated jet of aerosols issuing from the nozzle (discussed in Sec. 4.4) as well as after deposition of aerosols on a moving free surface (discussed in Sec. 4.5). In addition, the underlying phenomena behind pneumatic aerosol generation are explored in Sec. 4.6.

4.4 Investigation of the Aerosol Flow in the Deposition Head. Using the CFD model, several simulations were carried out to understand the underlying phenomena behind experimental observations. They were focused on the flow of material: (i) within the print head and nozzle; (ii) during the deposition on a free surface; and (iii) after the deposition (where the deposited aerosols experience the phenomena of coalescence, spreading, receding, relaxation, and wetting equilibrium [43]). Figure 13 depicts the influence of the ShGFR on the aerosol flow streamlines as well as velocity profile within the combination chamber.

As the ShGFR increases, the flow of aerosols gets more collimated in the form of a narrow beam, which is further accelerated when passing through the nozzle. Based on the aerosol flow diameter at the inlet and outlet of the combination chamber, a dimensionless variable is defined, called the *collimation ratio*, representing the ratio of the inlet flow diameter to the outlet flow diameter. An increase in the collimation ratio is observed from approximately 4 (at the ShGFR of 40 sccm) to 5 (at the ShGFR of 100 sccm).

To assess the stability of the aerosol flow, Reynolds number (Re) was monitored at the combination chamber exit as well as at the nozzle exit, plotted in Fig. 14 as a function of the ShGFR. It turned out that the collimated flow of aerosols would remain laminar even at the ShGFR of 100 sccm. This implies that stable material transfer and deposition happen with respect to the set experimental conditions (discussed in Table 1).

A comparison of the jet of aerosols (exiting from the nozzle) at the four levels of the ShGFR is demonstrated in Fig. 15. The jet width decreases as the ShGFR increases. This is an indication of narrower and thicker deposition of the material on the substrate (as observed experimentally in Sec. 4.3). We note that the streamlines ultimately diverge near the surface due to the surface barrier and pressure accumulation. This phenomenon gets less prominent as the collimation power (exerted by the sheath flow) increases from the ShGFR of 40 sccm to the ShGFR of 100 sccm.

4.5 Investigation of Aerosol Deposition on a Moving Free Surface. The impact of the aerosols on the substrate was investigated, utilizing the Weber number (We)—defined as the ratio of
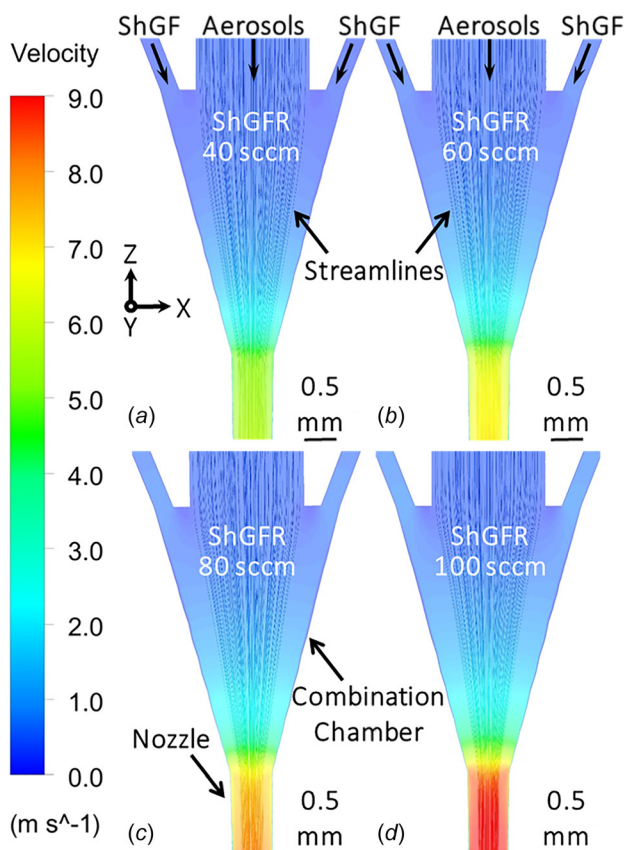
Fig. 13 Simulation of the collimation of aerosols within the deposition head with the aid of the sheath gas flow (ShGF). The aerosol flow is further accelerated by the nozzle before deposition.
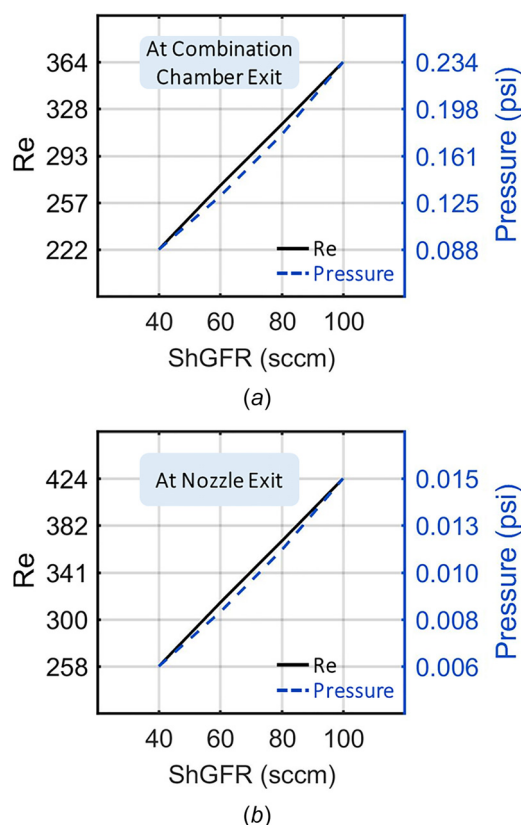
Fig. 14 Reynolds number (Re) versus ShGFR: (a) at the combination chamber exit and (b) at the nozzle exit. The aerosol flow remains laminar, indicative of stable aerosol transfer and deposition.
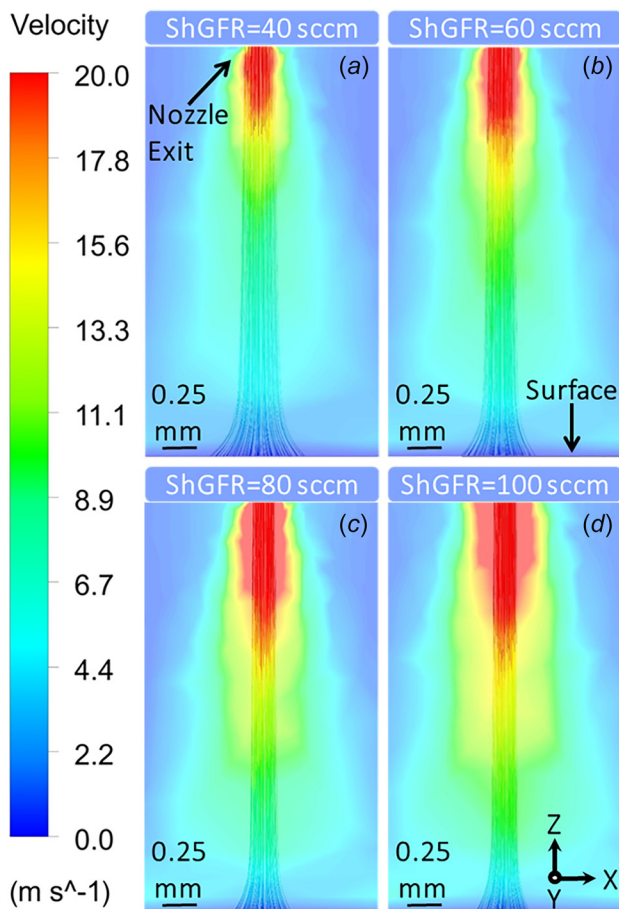
Fig. 15 Simulation of the deposition of aerosols on a free surface under the influence of the sheath flow. As the ShGFR increases, the jet width decreases, indicative of formation of narrower and thicker lines.

Fig. 16 Impingement of aerosols on a cold surface with film under various levels of the ShGFR. At large Weber numbers (≥ 2), the incoming aerosols stick to the substrate.

Fig. 17 Aerosol distortion from a spherical shape upon impingement on a surface versus ShGFR, captured using normalized displacement, based on the Taylor analogy breakup model. The edge aerosols experience less distortion.

aerodynamic forces to surface tension forces—as illustrated in Fig. 16. We note that there exists a wall film due to the continuous deposition of the aerosols. Since the substrate is not heated, the cold-wall-with-film model (also known as cold-wetting [53]) can properly reflect the physics behind the aerosol impingement. Under the presence of the wall film, when the Weber number is low (i.e., ≤ 2, at the ShGFR of 40 sccm and 60 sccm), the impinging aerosols are reflected. On the other hand, at high Weber numbers (observed at the ShGFR of 80 sccm and 100 sccm), the aerosols stick to the substrate and contribute to the wall film formation.

The Taylor analogy breakup (TAB) model [53]—where the droplet surface tension forces, drag force, and viscosity forces are analogous to the restoring force, external force, and damping force of a spring mass system, respectively—was employed for postdeposition analysis of the aerosol oscillation and distortion. Visualized in Fig. 17, the normalized displacement represents the displacement of the aerosol equator from its undisturbed position (normalized with respect to the initial, undisturbed equator). Note that those aerosols, deposited along the center of the line, are distorted much more significantly than the edge aerosols, remaining almost undistorted upon impingement. Consequently, the cross-sectional profile of the line would be nonuniform, as implied from Fig. 11. The magnitude of the distortion increases with the ShGFR.

The line morphology is adversely affected as the PS increases from 1 to 4 mm/s as illustrated in Fig. 18. This stems from the spreading effect of the PS, which deprives the impinging aerosols of initial wall film formation, subsequent coalescence, and ultimately formation of a continuous line trace. In addition, tracking the Weber number of the aerosols—defined as the ratio of the
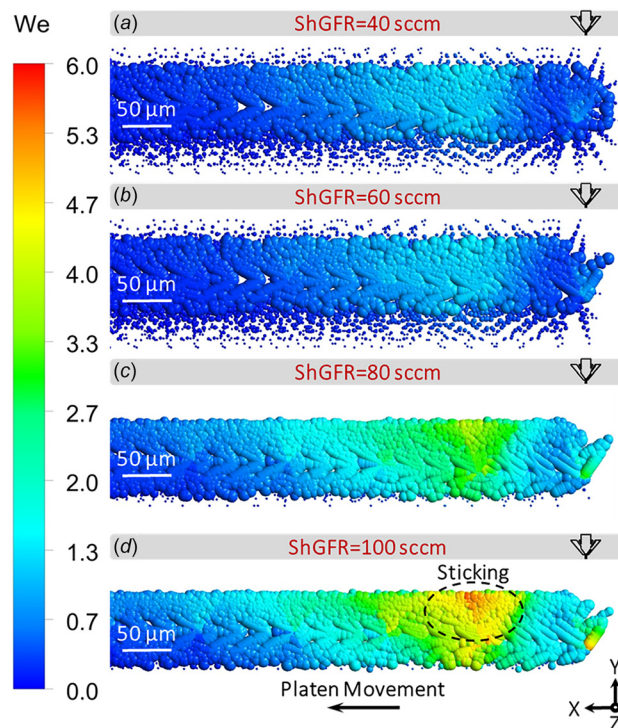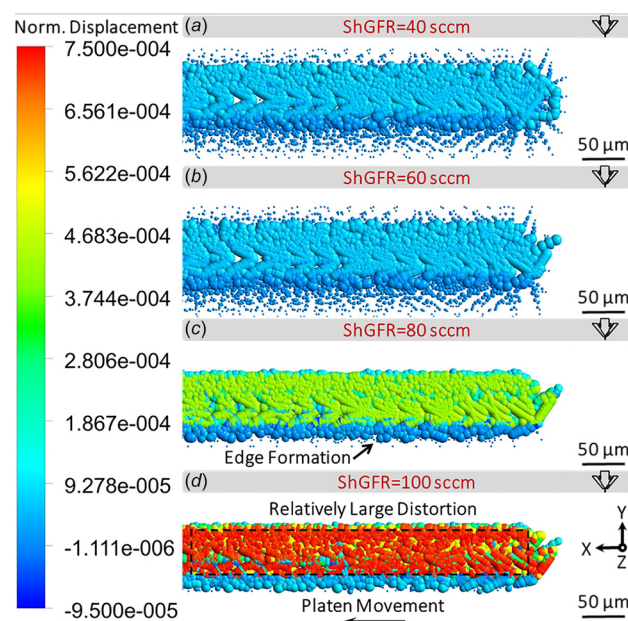
inertia of a fluid to the surface tension—revealed that the aerosols contribute to the formation of the thin wall film (and thus the line trace) less significantly when the PS increases.

4.6 Investigation of the Aerosol Flow in the Pneumatic Atomizer.
The objective of this section is to discuss the underlying physical phenomena behind pneumatic atomization (aerosol generation) in the AJP process.
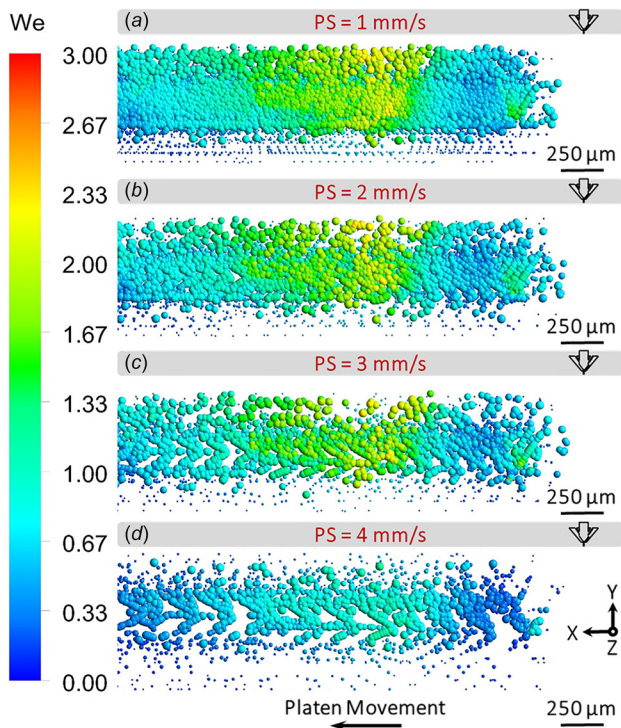
We

3.00
2.67
2.33
2.00
1.67
1.33
1.00
0.67
0.33
0.00

(a) PS = 1 mm/s

250 μm

(b) PS = 2 mm/s

250 μm

(c) PS = 3 mm/s

250 μm

(d) PS = 4 mm/s

250 μm

Platen Movement

Fig. 18 A CFD simulation of the influence of PS on AJ-printed trace morphology, demonstrating the impingement and postdeposition coalescence of aerosols on a moving free surface. An increase in the Weber number (We) is indicative of the fact that that the aerosols contribute to the line formation more significantly (by sticking to the wall film).

As discussed in Sec. 4.2, the physics (including the boundary conditions) of the model was setup based on experimental data. The veracity of the model was corroborated by: (i) setting experimental boundary conditions and (ii) obtaining a converged solution at the end of each transient simulation iteration. Please note

that obtaining real-time sensor data (which reflects the dynamics of the pneumatic atomizer), other than the presented data, is beyond the scope of this work. This requires sophisticated sensors, inserted within the atomizer, allowing for measuring the velocity and other properties of the atomization jet flow. Note that the sensor insertion should be implemented such that the main atomization stream remains undisturbed. Particle-size distribution can be captured utilizing image-based sensors.

Particle-size distribution is influenced by the jet velocity (fluid's inertia), ink viscosity, and ink surface tension. CFD simulation of the jet velocity allows for estimation of the particle-size distribution, which affects the morphology (and the functional properties) of AJ-deposited electronic devices. In addition, simulation of the velocity field of the atomization chamber—as a function of the orifice's and the capillary tube's diameter as well as of flow conditions, such as flow rate and pressure—would be critical from the atomizer design standpoint.

Having passed through the orifice, the AGF becomes completely turbulent, as implied from Fig. 19. This turbulent jet flow—having a Reynolds number (Re) of about 7000 at the orifice exit—breaks the ink, drawn upward based on the Venturi effect, into a nonuniform mist (cloud) of aerosols. The aerosols, subsequently, are carried toward the atomizer's outlet (and next, toward the virtual impactor) by the AGF. This flow experiences expansion twice: first at the orifice's exit (as a single phase flow, composed of N_2), and second at the atomization chamber's exit (as a two-phase flow of N_2 plus ink).

As exhibited in Fig. 20, the velocity field and the streamlines of both phases indicate the presence of not only a turbulent two-phase flow but also a vertex above the capillary tube (pertaining to the ink flow). This phenomenon emerges when the ink flow is sheared by the atomization jet, resulting in formation of aerosols. The streamlines of Phase II (i.e., ink) reflect randomness and thus turbulence in the atomization/nebulization process. In addition, they imply that a significant portion of the generated aerosols may be taken inward (back to the chamber) due to the occurrence of the vortex. It seems there is no ink flow above the atomization jet (acting as an aerodynamic barrier); however, due to the presence of turbulence, the aerosols are mixed with the AGF jet, and eventually carried toward the atomizer's outlet. Please note that the
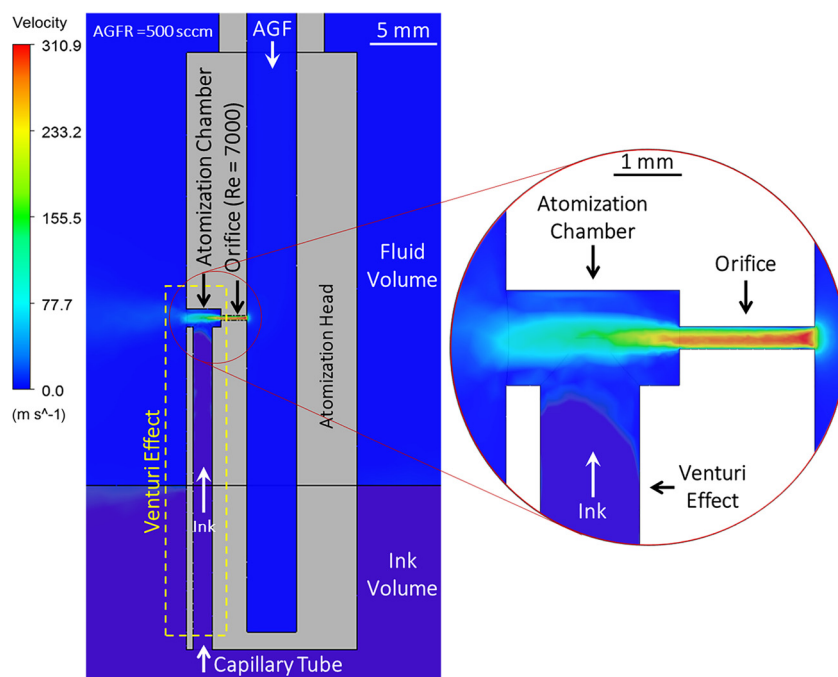

Fig. 19 The velocity field within the atomization head. The atomization jet (at the orifice exit) is turbulent, characterized with a Re of approximately 7000.
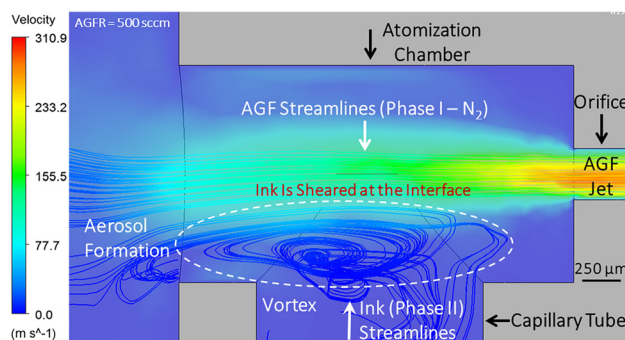
Fig. 20 The velocity field along with the streamlines of both Phase I and Phase II within the atomization chamber, demonstrating the presence of a turbulent, two-phase vortex flow above the capillary tube (leading to aerosol generation)

capillary tube's diameter (under constant atomization conditions) influences the momentum of ink delivery to the chamber (based on the Venturi effect), the resulting ink vortex, and ultimately the rate of aerosol generation.

Demonstrated in Fig. 21, the velocity vectors of Phase I reveal another phenomenon, i.e., the occurrence of circulation above the atomization jet. This is indicative of the fact that some of the fluid in the atomizer is taken inward (back to the atomization chamber) from both the upper and the lower edges. However, the lower intake flow is much less significant than the upper one due to the presence of the capillary tube and thus ink volume in that region. Please note that this phenomenon is in addition to the intake flow resulting from the vortex.

Furthermore, the orifice's diameter influences the dynamics of the issuing jet. For example, as implied from Fig. 21, increasing the diameter would result in less (narrower) circulation and less significant flow intake toward the atomization chamber. Also, under constant atomization conditions, this would lead to more significant turbulent flow (according to Reynolds number), affecting the particle-size distribution.

As shown in Fig. 22, the ink in the capillary tube is drawn upward due to the Venturi effect (as a result of reduction in the fluid pressure). There is a rapid transition in the flow regime from *developing* to *fully developed*. This can be attributed to the fact that the ink flow is a viscous flow (the ink viscosity is approximately 50 cP). In addition, this phenomenon is implicitly apparent from the graph illustrated in Fig. 22, where the ink flow velocity initially increases (indicative of the developing region) and then approximately levels off (indicative of the fully developed region; this region is mathematically described as $\frac{\partial w}{\partial z} = 0$, where w is the
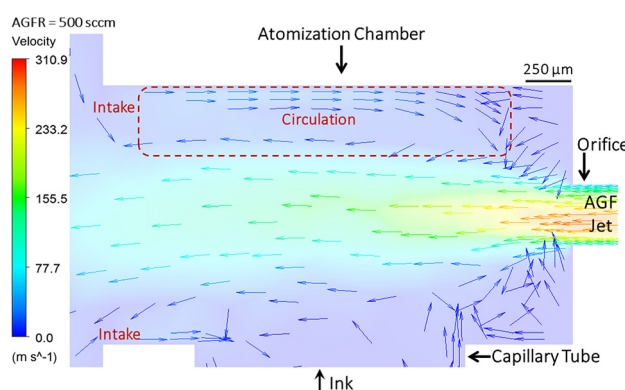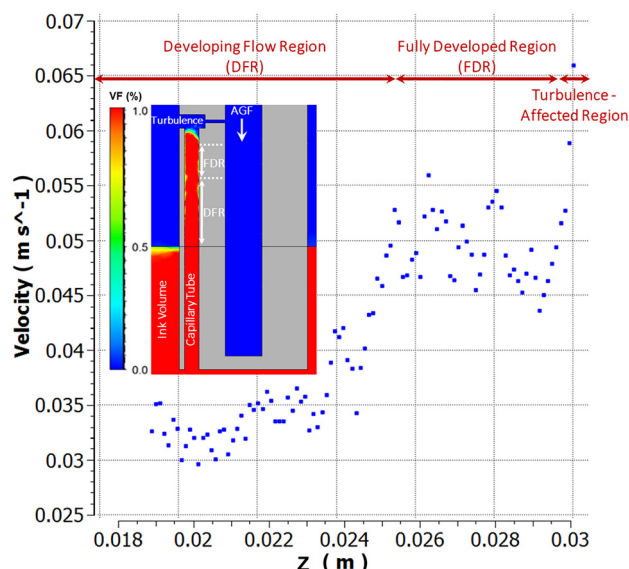

Fig. 22 The ink (Phase II) velocity as a function of elevation (*z*) within the capillary tube (above the ink level). The ink flow becomes fully developed rapidly, being under the influence of viscosity (the ink viscosity is about 50 cP). Belonging to the last time-step, all the points were sampled along the centerline of the capillary tube from the developing flow region (DFR) to the fully developed region (FDR) as shown by two arrows on the volume fraction (VF) contour.

z-component of velocity vector, **V**. Once the ink flow has reached the turbulent region (at the end of the capillary tube), the velocity starts rising again in a random fashion.

Please note that the length of the hydrodynamic entry region, *L*, where the flow is developing, is mathematically expressed as

$$L = 0.06 \frac{\rho \mathbf{v} D^2}{\mu} \qquad (16)$$

In Eq. (16), ρ is the fluid density [kg/m^3]; $\mathbf{v}$ is the velocity vector [m/s]; D is the characteristic length (i.e., diameter) [m]; and μ is the fluid dynamic viscosity [mPa · s]. Please note that as the dynamic viscosity of a fluid increases, the length of the hydrodynamic entry region, *L*, decreases.

Salary et al. [22] demonstrated that optimal material deposition regimes exist when the ShGFR is in the range of 40–100 sccm. The veracity of this observation was corroborated in this study

Fig. 21 Normalized velocity vectors within the atomization chamber, revealing the presence of asymmetric flow intake and circulation
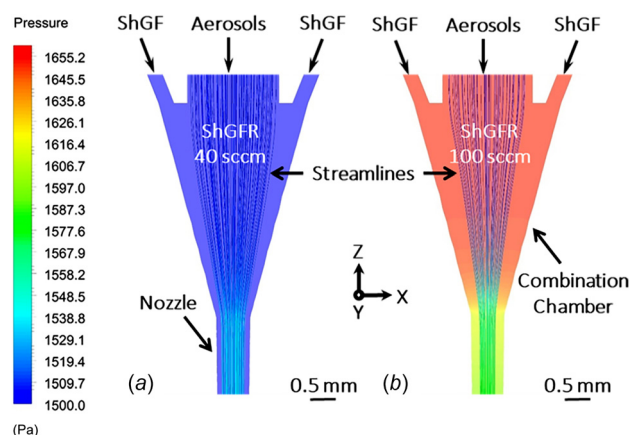

Fig. 23 The influence of the ShGFR (at two levels of 40 sccm and 100 sccm) on the flow pressure as well as the aerosol flow streamlines in the deposition head

where it was shown that when the ShGFR increases (from 40 to 100 sccm), more focused and stable material deposition occurs leading to dense deposition of aerosols with almost no formation of overspray (as implied from Figs. 11 and 16). Furthermore, pressure accumulation and nozzle clog at high ShGFRs (> 100 sccm) were reported in [22]. As illustrated in Fig. 23, while the flow pressure in the deposition head increases as a result of an increase in the ShGFR, the aerosol flow streamlines still remain intact, confirming the existence of an optimal process operability regime in the range of 40-100 sccm. In addition, the trend shown in Fig. 18 implies that electronic traces (lines) with optimal morphological characteristics are obtained when the PS is at 1 mm/s; this trend is consistent with the experimentally observed trend (discussed in Ref. [22]), which concluded that a PS in the range of 1–1.5 mm/s would lead to optimal line morphology.

5 Conclusion and Future Work

5.1 Conclusions. In this work, a 3D compressible, turbulent, multiphase flow CFD model was forwarded to investigate the aerodynamics behind: (i) aerosol generation (aerosolization), (ii) aerosol transport (within the deposition head), and (iii) aerosol deposition (on a moving free surface) in the AJP process. A factorial experiment (consisting of AJ-deposition of silver nanoparticles on a polyimide substrate) was conducted to observe the influence of ShGFR on line morphology, and also to validate the accuracy of the CFD model. A good agreement between the CFD prediction of line morphology and the experimental measurements was observed. The following conclusions were deduced from the results of this study:

- As the ShGFR increases, the flow of aerosols gets more collimated in the form of a narrow beam, which is further accelerated when passing through the nozzle. As a result, narrower and thicker structures are deposited on a substrate.
- Under the presence of wall film, at low Weber numbers, the impinging aerosols are reflected, while at high Weber numbers, they stick to the substrate and contribute to the wall film formation.
- The edge aerosols remain almost undistorted upon impingement, while those deposited along the line center, are distorted much more remarkably.
- The atomization gas flow experiences expansion twice: (i) at the orifice's exit; and (ii) at the chamber's exit. The atomization gas flow becomes completely turbulent once it has passed through the orifice. This turbulent flow breaks the ink flow into a nonuniform mist of aerosols.
- It turned out that there would be a turbulent, two-phase flow as well as a vertex above the capillary tube in the atomization chamber. Due to the presence of the vortex, a significant portion of the generated aerosols is pulled back toward the atomization chamber. In addition, some of the fluid in the atomizer is, additionally, drawn toward the chamber due to the occurrence of circulation above the atomization jet.
- The ink flow in the capillary tube becomes *fully developed* swiftly. However, once the ink flow has reached the turbulent region, the velocity starts climbing randomly.

5.2 Future Work. Nebulization in the AJP process results in formation of aerosols, typically having a diameter of 1–5 μm. In order to observe the distribution of aerosols, the flow domain should be meshed with micro-elements (cells), which make the CFD model computationally expensive. This challenge will be addressed as part of the authors' future work. Furthermore, the effects of compressibility (in terms of density and pressure changes) during atomization will be investigated. This CFD study will be expanded with incorporation of more critical AJP process parameters, such as nozzle size as well as ink properties (viscosity, solvent evaporation, etc.).

Nomenclature

$\mathcal{A}$ = area
$C_{D\mathbf{g}}$ = drag coefficient
$C_{\mathbf{v}}$ = heat capacity at constant volume
C_{VM} = virtual mass factor
C_{μ} = turbulent viscosity constant
D = characteristic length
d_D = particle diameter
$\mathbf{F}_{Dg}$ = drag force per unit particle mass
$\mathbf{F}_{g}$ = gravitational force per unit particle mass
$\mathbf{F}_{PG}$ = pressure gradient force per unit particle mass
$\mathbf{F}_{SL}$ = Saffman lift force per unit particle mass
$\mathbf{F}_{VM}$ = virtual mass force per unit particle mass
$\mathbf{g}$ = gravitational acceleration vector
k = fluid turbulence kinetic energy
$\mathbf{n}$ = surface normal vector
p = fluid pressure
$\mathrm{Pr}_{\varepsilon}$ = turbulence dissipation rate Prandtl number
Pr_k = turbulence kinetic energy Prandtl number
R = universal gas constant
Re = Reynolds number
S = rate of strain of fluid elements
S_E = energy source term
S_M = momentum source term
S_k = turbulence kinetic energy source term
S_{ε} = turbulence dissipation rate source term
T = fluid temperature
T = time
u = x-component of the fluid velocity vector
$\mathbf{v}$ = y-component of the fluid velocity vector
$\mathcal{V}$ = volume
$\mathbf{v}$ = velocity vector
v = mean velocity vector
$\mathbf{v}_D$ = discrete phase (particle) velocity vector
w = z-component of the fluid velocity vector
We = Weber number
y^* = nondimensionalized distance from a wall

Greek Symbols

ε = turbulence dissipation rate
ε_D = turbulence dilatation dissipation rate
κ = fluid thermal conductivity
μ = fluid dynamic viscosity

μ_t = turbulent/eddy viscosity
ρ = fluid density
ρ_D = discrete phase density
τ_w = wall shear stress
Φ = dissipation function
ω_k = angular velocity of the system of rotation
$\overline{\Omega}_{ij}$ = mean rate of rotation tensor

Aerosol Jet Printing Terms

AGF = atomization gas flow
AGFR = atomization gas flow rate
CC = combination chamber
CT = computed tomography
DPM = discrete phase model
EGF = exhaust gas flow
EGFR = exhaust gas flow rate
LPC = lower plenum chamber
PA = pneumatic atomizer
PS = print speed
ShGF = sheath gas flow
ShGFR = sheath gas flow rate
UA = ultrasonic atomizer
UPC = upper plenum chamber
VI = virtual impactor

References

[1] Krzeminski, J., Wroblewski, G., Dybowska-Sarapuk, L., Lepak, S., and Jakubowska, M., 2017, "Nanosilver Conductive Lines Made by Spray Coating and Aerosol Jet Printing Technique," Proceedings of the Photonics Applications in Astronomy, Communications, Industry, and High Energy Physics Experiments 2017, International Society for Optics and Photonics, Wilga, Poland, Aug. 7, p. 1044555.

[2] Seifert, T., Baum, M., Roscher, F., Wiemer, M., and Gessner, T., 2015, "Aerosol Jet Printing of Nano Particle Based Electrical Chip Interconnects," Mater. Today: Proc., 2(8), pp. 4262–4271.

[3] Vogeler, F., Verheecke, W., Voet, A., and Valkenaers, H., 2013, "An Initial Study Into Aerosol Jet Printed Interconnections on Extrusion Based 3D Printed Substrates," Strojniski Vestnik-J. Mech. Eng., 59(11), pp. 689–696.

[4] Reitberger, T., Franke, J., Hoffmann, G.-A., Overmeyer, L., Lorenz, L., and Wolter, K.-J., 2016, "Integration of Polymer Optical Waveguides by Using Flexographic and Aerosol Jet Printing," Proceedings of the 12th International Congress Molded Interconnect Devices (MID), Würzburg, German, Sept. 28–29, IEEE, pp. 1–6.

[5] Reitberger, T., Hoffmann, G.-A., Wolfer, T., Overmeyer, L., and Franke, J., 2016, "Printing Polymer Optical Waveguides on Conditioned Transparent Flexible Foils by Using the Aerosol Jet Technology," Proceedings of Printed Memory and Circuits II, San Diego, CA, Aug. 28–Sept. 1, p. 99450G.

[6] Eckstein, R., Hernandez-Sosa, G., Lemmer, U., and Mechau, N., 2014, "Aerosol Jet Printed Top Grids for Organic Optoelectronic Devices," Org. Electron., 15(9), pp. 2135–2140.

[7] Rudorfer, A., Tscherner, M., Palfinger, C., Reil, F., Hartmann, P., Seferis, I. E., Zych, E., and Wenzl, F. P., 2016, "A Study on Aerosol Jet Printing Technology in LED Module Manufacturing," Proceeding of the Fifteenth International Conference on Solid State Lighting and LED-Based Illumination Systems, San Diego, CA, Aug. 28–Sept. 1, p. 99540E.

[8] Tait, J. G., Witkowska, E., Hirade, M., Ke, T.-H., Malinowski, P. E., Steudel, S., Adachi, C., and Heremans, P., 2015, "Uniform Aerosol Jet Printed Polymer Lines With 30 μm Width for 140ppi Resolution RGB Organic Light Emitting Diodes," Org. Electron., 22, pp. 40–43.

[9] Oh, Y. S., Lee, K. H., Jung, J. H., Ko, S. H., and Sung, H. J., 2012, "Multicolor Luminescent Patterns of Quantum Dot Through Real-Time Controlling," Proceedings of the 14th Korean MEMS Conference (FP-1-35), Jeju, South Korea, Apr. 5, pp. 5–7.

[10] Wang, S.-W., Lin, H.-Y., Lin, C.-C., Kao, T. S., Chen, K.-J., Han, H.-V., Li, J.-R., Lee, P.-T., Chen, H.-M., Hong, M.-H., and Kuo, H.-C., 2016, "Pulsed-Laser Micropatterned Quantum-Dot Array for White Light Source," Sci. Rep., 6(1), p. 23563.

[11] Goth, C., Putzo, S., and Franke, J., "Aerosol Jet Printing on Rapid Prototyping Materials for Fine Pitch Electronic Applications," Proceeding of the IEEE Electronic Components and Technology Conference (ECTC), Lake Buena Vista, FL, 31 May–03 June, pp. 1211–1216.

[12] Liu, R., Ding, H., Lin, J., Shen, F., Cui, Z., and Zhang, T., 2012, "Fabrication of Platinum-Decorated Single-Walled Carbon Nanotube Based Hydrogen Sensors by Aerosol Jet Printing," Nanotechnology, 23(50), p. 505301.

[13] Zhao, D., Liu, T., Zhang, M., Liang, R., and Wang, B., 2012, "Fabrication and Characterization of Aerosol-Jet Printed Strain Sensors for Multifunctional Composite Structures," Smart Mater. Struct., 21(11), p. 115008.

[14] Jones, C. S., Lu, X., Renn, M., Stroder, M., and Shih, W.-S., 2010, "Aerosol-Jet-Printed, High-Speed, Flexible Thin-Film Transistor Made Using Single-Walled Carbon Nanotube Solution," Microelectron. Eng., 87(3), pp. 434–437.

[15] Kim, S. H., Hong, K., Lee, K. H., and Frisbie, C. D., 2013, "Performance and Stability of Aerosol-Jet-Printed Electrolyte-Gated Transistors Based on Poly (3-Hexylthiophene)," ACS Appl. Mater. Interfaces, 5(14), pp. 6580–6585.

[16] Liu, R., Shen, F., Ding, H., Lin, J., Gu, W., Cui, Z., and Zhang, T., 2013, "All-Carbon-Based Field Effect Transistors Fabricated by Aerosol Jet Printing on Flexible Substrates," J. Micromech. Microeng., 23(6), p. 065027.

[17] Hon, K., Li, L., and Hutchings, I., 2008, "Direct Writing Technology—Advances and Developments," CIRP Ann.-Manuf. Technol., 57(2), pp. 601–620.

[18] King, B., and Renn, M., 2009, "Aerosol Jet Direct Write Printing for Mil-Aero Electronic Applications," Proceedings of the Lockheed Martin Palo Alto Colloquia, Palo Alto, CA, Mar. 26, pp. 1–6.

[19] Parekh, D. P., Cormier, D., and Dickey, M. D., 2015, "Chapter 8: Multifunctional Printing: Incorporating Electronics Into 3D Parts Made by Additive Manufacturing," Additive Manufacturing, A. Ban, dyopadhyay, and S. Bose, eds., CRC Press, Boca Raton, FL, p. 215.

[20] Salary, R., Lombardi, J. P., Weerawarne, D. L., Tootooni, M. S., Rao, P. K., and Poliks, M. D., 2020, "A Sparse Representation Classification Approach for Near Real-Time, Physics-Based Functional Monitoring of Aerosol Jet-Fabricated Electronics," ASME J. Manuf. Sci. Eng., 142(8), p. 081007.

[21] Salary, R., Lombardi, J., Rao, P., and Poliks, M. D., 2017, "Online Monitoring of Functional Electrical Properties in Aerosol Jet Printing Additive Manufacturing Process Using Shape-From-Shading Image Analysis," ASME J. Manuf. Sci. Eng., 139(10), p. 101010.

[22] Salary, R., Lombardi, J. P., Tootooni, M. S., Donovan, R., Rao, P. K., Borgesen, P., and Poliks, M. D., 2017, "Computational Fluid Dynamics Modeling and Online Monitoring of Aerosol Jet Printing Process," ASME J. Manuf. Sci. Eng., 139(2), p. 021015.

[23] Wadhwa, A., 2015, "Run-Time Ink Stability in Pneumatic Aerosol Jet Printing Using a Split Stream Solvent Add Back System," M.S. thesis, Advisor: Denis Cormier, Department of Industrial and Systems Engineering, Rochester Institute of Technology, Rochester, NY.

[24] Lombardi, J. P., Salary, R., Weerawarne, D. L., Rao, P. K., and Poliks, M. D., 2018, "In Situ Image-Based Monitoring and Closed-Loop Control of Aerosol Jet Printing," ASME Paper No. 6487.

[25] Salary, R., Lombardi, J. P., Rao, P. K., and Poliks, M. D., 2017, "Additive Manufacturing (AM) of Flexible Electronic Devices: Online Monitoring of 3D Line Morphology in Aerosol Jet Printing Process Using Shape-From-Shading Image Analysis," ASME Paper No. 2947.

[26] Salary, R., Lombardi, J. P., Tootooni, M. S., Donovan, R., Rao, P. K., and Poliks, M. D., 2016, "In Situ Sensor-Based Monitoring and Computational Fluid Dynamics (CFD) Modeling of Aerosol Jet Printing (AJP) Process," ASME Paper No. 8535.

[27] Salary, R., Lombardi, J. P., Weerawarne, D. L., Tootooni, M. S., Rao, P. K., and Poliks, M. D., 2018, "In Situ Functional Monitoring of Aerosol Jet Printed Electronic Devices Using a Combined Sparse Classification Approach," ASME Paper No. 6586.

[28] Salary, R., Lombardi, J. P., Weerawarne, D. L., Rao, P. K., and Poliks, M. D., 2018, "A Computational Fluid Dynamics (CFD) Study of Material Transport and Deposition in Aerosol Jet Printing (AJP) Process," ASME Paper No. 87647.

[29] Salary, R., Lombardi, J. P., Weerawarne, D. L., Rao, P. K., and Poliks, M. D., 2018, "A State-of-the-Art Review on Aerosol Jet Printing (AJP) Additive Manufacturing Process," ASME Paper No. 3008.

[30] Wang, K., Chang, Y.-H., Zhang, C., and Wang, B., 2016, "Conductive-on-Demand: Tailorable Polyimide/Carbon Nanotube Nanocomposite Thin Film by Dual-Material Aerosol Jet Printing," Carbon, 98, pp. 397–403.

[31] Efimov, A., Arsenov, P., Protas, N., Minkov, K., Urazov, M., and Ivanov, V., 2017, "Dry Aerosol Jet Printing of Conductive Silver Lines on a Heated Silicon Substrate," Proceeding of the IOP Conference Series: Materials Science and Engineering, International Conference on Mechanical Engineering and Applied Composite Materials, IOP Publishing, Hong Kong, Nov. 23–24, p. 012082.

[32] Efimov, A., Arsenov, P., Volkov, I., Urazov, M., and Ivanov, V., 2017, "Study of Aerosol Jet Printing With Dry Nanoparticles Synthesized by Spark Discharge," IOP Conf. Series: J. Phys.: Conf. Series, 917(9), p. 092020.

[33] Gu, Y., Gutierrez, D., Das, S., and Hines, D., 2017, "Inkwells for on-Demand Deposition Rate Measurement in Aerosol-Jet Based 3D Printing," J. Micromech. Microeng., 27(9), p. 097001.

[34] Chang, Y.-H., 2017, "Process Monitoring, Modeling, and Quality Assessment for Printed Electronics With Aerosol Jet Printing Technology," Ph.D. dissertation, Advisor: Dr. Ben Wang, H. Milton Stewart School of Industrial and Systems Engineering, Georgia Institute of Technology, Atlanta, GA.

[35] Thompson, B., and Yoon, H.-S., 2015, "Velocity-Regulated Path Planning Algorithm for Aerosol Printing Systems," ASME J. Manuf. Sci. Eng., 137(3), p. 031020.

[36] Smith, M., Choi, Y. S., Boughey, C., and Kar-Narayan, S., 2017, "Controlling and Assessing the Quality of Aerosol Jet Printed Features for Large Area and Flexible Electronics," Flexible Printed Electron., 2(1), p. 015004.

[37] Sun, H., Wang, K., Li, Y., Zhang, C., and Jin, R., 2017, "Quality Modeling of Printed Electronics in Aerosol Jet Printing Based on Microscopic Images," ASME J. Manuf. Sci. Eng., 139(7), p. 071012.

[38] Li, Y., Mohan, K., Sun, H., and Jin, R., 2017, "Ensemble Modeling of In Situ Features for Printed Electronics Manufacturing With In Situ Process Control Potential," IEEE Rob. Autom. Lett., 2(4), pp. 1864–1870.

[39] Verheecke, W., Van Dyck, M., Vogeler, F., Voet, A., and Valkenaers, H., 2012, "Optimizing Aerosol Jet Printing of Silver Interconnects on Polyimide Film for

Embedded Electronics Applications," Proceedings of the Eighth International DAAAM Baltic Conference Danube Adria Association for Automation and Manufacturing (DAAAM), Tallinn, Estonia, Apr. 19–21, pp. 373–379.

[40] Mahajan, A., Frisbie, C. D., and Francis, L. F., 2013, "Optimization of Aerosol Jet Printing for High-Resolution, High-Aspect Ratio Silver Lines," ACS Appl. Mater. Interfaces, **5**(11), pp. 4856–4864.

[41] Chen, G., Gu, Y., Tsang, H., Hines, D. R., and Das, S., 2018, "The Effect of Droplet Sizes on Overspray in Aerosol-Jet Printing," Adv. Eng. Mater., **20**(8), pp. 1701084–1701084.

[42] Feng, J. Q., 2015, "Sessile Drop Deformations Under an Impinging Jet," Theor. Comput. Fluid Dyn., **29**(4), pp. 277–290.

[43] Feng, J. Q., 2016, *A Computational Study of High-Speed Microdroplet Impact Onto a Smooth Solid Surface*, Cornell University Library, Physics-Fluid Dynamics, Xiv:1602.07672, Ithaca, NY.

[44] Feng, J. Q., 2018, "A Computational Analysis of Gas Jet Flow Effects on Liquid Aspiration in the Collison Nebulizer," Preprints, 2018020128.

[45] Schulz, D., Hoey, J., Thompson, D., Swenson, O., Han, S., Lovaasen, J., Dai, X., Braun, C., Keller, K., and Akhatov, I., 2008, "Collimated Aerosol Beam Deposition: Sub 5-μm Resolution of Printed Actives and Passives," Proceedings of the Flexible Electronics and Displays Conference and Exhibition, Phoenix, AZ, Jan. 21–24, pp. 1–8.

[46] Akhatov, I., Hoey, J., Swenson, O., and Schulz, D., 2008, "Aerosol Focusing in Micro-Capillaries: Theory and Experiment," J. Aerosol Sci., **39**(8), pp. 691–709.

[47] Akhatov, I., Hoey, J., Swenson, O., and Schulz, D., 2008, "Aerosol Flow Through a Long Micro-Capillary: Collimated Aerosol Beam," Microfluid. Nanofluid., **5**(2), pp. 215–224.

[48] Akhatov, I. S., Hoey, J. M., Thompson, D., Lutfurakhmanov, A., Mahmud, Z., Swenson, O. F., Schulz, D. L., and Osiptsov, A. N., 2009, "Aerosol Flow Through a Micro-Capillary," Proceeding of the Second International Conference on Micro/Nanoscale Heat and Mass Transfer, Shanghai, China, Dec. 18–21, pp. 223–232.

[49] May, K., 1973, "The Collison Nebulizer: Description, Performance and Application," J. Aerosol Sci., **4**(3), pp. 235–243.

[50] Hoey, J. M., Lutfurakhmanov, A., Schulz, D. L., and Akhatov, I. S., 2012, "A Review on Aerosol-Based Direct-Write and Its Applications for Microelectronics," J. Nanotechnol., **2012**, pp. 1–22.

[51] Renn, M. J., Christenson, K. K., Giroux, D., Resin Designs, L., and Blazej, D., 2013, "Aerosol Jet Printing of Conductive Epoxy for 3D Packaging," Proceeding of Pan Pacific Microelectronics Symposium (PAN PAC 2013), Maui, HI, Jan. 22–24, pp. 1–7.

[52] King, B. H., Renn, M. J., and Paulsen, J. A., 2011, "Miniature Aerosol Jet and Aerosol Jet Array," Optomec Inc., Albuquerque, NM, U.S. Patent No. US7938341B2 (U.S. Patent and Trademark Office, Washington, DC).

[53] ANSYS-Fluent, 2015, "16.2 Theory Guide," ANSYS, Canonsburg, PA.

[54] Versteeg, H. K., and Malalasekera, W., 2007, *An Introduction to Computational Fluid Dynamics: The Finite Volume Method*, 2nd ed., Pearson Education in South Asia, Noida, India.

[55] Shih, T.-H., Liou, W. W., Shabbir, A., Yang, Z., and Zhu, J., 1995, "A New k-ϵ Eddy Viscosity Model for High Reynolds Number Turbulent Flows," Comput. Fluids, **24**(3), pp. 227–238.

[56] Launder, B. E., and Spalding, D. B., 1974, "The Numerical Computation of Turbulent Flows," Comput. Methods Applied Mechanics Engineering, **3**(2), pp. 269–289.

[57] Gosman, A., and Loannides, E., 1983, "Aspects of Computer Simulation of Liquid-Fueled Combustors," J. Energy, **7**(6), pp. 482–490.

[58] Saffman, P., 1965, "The Lift on a Small Sphere in a Slow Shear Flow," J. Fluid Mech., **22**(2), pp. 385–400.

[59] Li, A., and Ahmadi, G., 1992, "Dispersion and Deposition of Spherical Particles From Point Sources in a Turbulent Channel Flow," Aerosol Sci. Technol., **16**(4), pp. 209–226.

[60] Lombardi, J. P., Salary, R. R., Weerawarne, D. L., Rao, P. K., and Poliks, M. D., 2019, "Image-Based Closed-Loop Control of Aerosol Jet Printing Using Classical Control Methods," ASME J. Manuf. Sci. Eng., **141**(7), p. 071011.